

VIETNAM NATIONAL UNIVERSITY, HANOI
UNIVERSITY OF ENGINEERING AND TECHNOLOGY



NGUYEN THU HANG

**SIMULATION STUDY ON A DUAL-AXIS THERMAL
CONVECTIVE GAS GYROSCOPE BASED ON CORONA
DISCHARGE ION WIND**

Field: Electronics and Telecommunications
Major: Electronic Engineering
Code: 60520203

MASTER THESIS IN

ELECTRONICS AND COMMUNICATIONS

Supervisor: Assoc. Prof. Bui Thanh Tung

HANOI - 2021

VIETNAM NATIONAL UNIVERSITY, HANOI
UNIVERSITY OF ENGINEERING AND TECHNOLOGY

NGUYEN THU HANG

**SIMULATION STUDY ON A DUAL-AXIS THERMAL
CONVECTIVE GAS GYROSCOPE BASED ON CORONA
DISCHARGE ION WIND**

Field: Electronics and Telecommunications
Major: Electronic Engineering
Code: 60520203

MASTER THESIS IN
ELECTRONICS AND COMMUNICATIONS

Supervisor: Assoc. Prof. Bui Thanh Tung

HANOI - 2021

AUTHORSHIP

“I hereby declare that the work entitled “Simulation study on a dual-axis thermal convective gas gyroscope based on corona discharge ion wind” contained in this thesis is of my own and has not been previously submitted for a degree or diploma at this or any other higher education institution. To the best of my knowledge and belief, the thesis contains no materials previously published or written by another person except where due reference or acknowledgement is made.”

Date: May 25, 2021

Signature:

ACKNOWLEDGEMENT

First of all, I would like to express my special thanks of gratitude to Assoc. Prof. Bui Thanh Tung, my beloved research supervisor, for his patient guidance, enthusiastic encouragement, and valuable support on this project. His passion, inspiration, insightful recommendations have been helping me overcome the difficulties that I encountered in all the researching and thesis writing time.

I would also like to extend my sincere thanks to Prof. Chu Duc Trinh, Dr. Dau Thanh Van, and Ph.D. student Tran Van Ngoc for giving me strength and their assistance at every stage of the research project.

In addition, I would like to show my appreciation to Micro-Electromechanical and Microsystems Department (MEMS), and the University of Engineering and Technology, for giving me a perfect working and researching environment.

Last but not least, I would like to offer my special thanks to my family and my friends for helping me a lot throughout writing this thesis and my life in general.

May 25, 2021

TABLE OF CONTENTS

Authorship	i
Acknowledgement.....	ii
Table of Contents	1
List of Figures	3
Abbreviation.....	4
Abstract	5
Chapter 1. Introduction	6
1.1. Gyroscopes and Applications.....	6
1.2. Classification of Gyroscopes.....	7
1.2.1. Mechanical Gyroscopes.....	7
1.2.2. Optical Gyroscopes.....	9
1.2.3. Micro-Electro-Mechanical (MEMS) Gyroscopes	11
1.2.4. Fluid Gyroscopes	13
1.3. Contributions and Thesis Overview	15
Chapter 2. Design and Principle of Proposed Gas Gyroscope	16
2.1. Corona Discharge Ionic Wind.....	16
2.2. Coriolis Effect	18
2.3. Thermal Convection	19
2.4. Bridge Measurement Circuit	20
2.5. Gas Gyroscopes Working Principle	22
Chapter 3. Simulation Study	24
3.1. Finite Element Method.....	24
3.2. COMSOL Multiphysics Software	26
3.3. Simulation Model	27
3.4. Numerical Model.....	27
Chapter 4. Results and Discussion	31
4.1. Simulation Results and Discussion.....	31
4.1.1. Velocity Profile.....	31

4.1.2. Temperature Distribution	32
4.2. Experimental Verification	34
Conclusion.....	36
Related Publications.....	37
Reference.....	38

LIST OF FIGURES

Figure 1-1: Angular velocity measurement system diagram	6
Figure 1-2: Gyroscopes applications [20]	6
Figure 1-3: Mechanical gyroscopes structure [22]	8
Figure 1-4: Mechanical gyroscopes [2]	8
Figure 1-5: Sagnac effects [27]	9
Figure 1-6: Optical gyroscopes classification [2]	10
Figure 1-7: Laser ring optical gyroscopes configuration [36]	11
Figure 1-8: Interferometric fiber optic gyroscopes working diagram [38]	11
Figure 1-9: Coriolis effect [43]	12
Figure 1-10: MEMS gyroscopes [45]	12
Figure 1-11: Jet flow gyroscopes [52]	13
Figure 1-12: Cut view of dual-axis jet flow gyroscope and graph of sensing element [53]	14
Figure 1-13: Thermal gas gyroscopes [54]	14
Figure 2-1: I-V Characteristics of glow discharge [55]	16
Figure 2-2: Corona induced ionic wind principle [60]	17
Figure 2-3: Needle-to-ring configuration [61]	17
Figure 2-4: Coriolis effect [79]	19
Figure 2-5: Forced convection and natural convection [81]	19
Figure 2-6: Thermistor temperature characteristics curve [80]	20
Figure 2-7: Wind sensor-based thermal resistors schematic and temperature distribution of sensor [72]	21
Figure 2-8: Wheatstone bridge circuit [73]	22
Figure 2-9: Gas gyroscope working principle	23
Figure 3-1: A three-dimensional finite element mesh generator [78]	24
Figure 3-2: Node geometry for two dimension and three dimension elements [78]	25
Figure 3-3: Second-order elements [78]	25
Figure 3-4: Mesh adaption to the droplet movement [78]	26
Figure 3-5: COMSOL Multiphysics software user interface [78]	26
Figure 3-6: Simulation model	27
Figure 3-7: Meshing model and boundary condition	30

ABBREVIATION

FEM	Finite Element Method
DC	Direct Current
MEMS	MicroElectroMechanical System
RLG	Ring Laser Gyroscopes
IFOG	Interferometric Fiber Optic Gyroscopes

ABSTRACT

Gyroscopes are devices used to measure the angular velocity of an object concerning an inertial frame of reference. It can be seen that gyroscopes have attracted tremendous attention from researchers and have emerged as useful devices in plenty of applications in abundant fields, such as robotics, military, aeronautics and astronautics, mobile phone, medical, smart home,... There are different approaches to the research and development of gyroscopes which can be listed as conventional mechanical gyroscopes, optical gyroscopes, microelectromechanical gyroscopes. Mechanical gyroscopes and optical gyroscopes have the advantage of high accuracy; however, these mentioned gyroscopes are too expensive and large to apply in some recently popular applications. Especially, optical gyroscopes which are bulky and require optical instruments are not easily integrated into MEMS systems. Due to the advancement of fabrication technology, the MEMS gyroscopes have the advantages of high performance, reasonable price, small size. Nevertheless, MEMS gyroscopes use proof mass as a vibrating element, leading to disadvantages of low shock resistance, fragility. In fabricating MEMS gyroscopes, the resonant frequency of two vibrating modes is one of the most important design factors. The unwanted vibration of mass also results in an undesired signal.

To address these problems, fluid gyroscopes which employ gas or a liquid as moving and sensing elements have been proposed. In this thesis, corona discharge ionic wind is used as jet flow due to the advantages of stability, easy integration, no moving parts requirement, no impoverishment. The applied angular rate is sensed by the change of thermal distribution in the working chamber resulted from the deflection of jet flow. The asymmetric thermal distribution is measured by the thermosensitive effect using a bridge circuit. The principle of this dual-axis thermal convective gas gyroscope based on corona discharge ion wind is extensively studied in this thesis. A numerical study and simulation model are presented to confirm the phenomenon and working principle of this gas gyroscope. The simulation results show good agreement with our research group's experimental results. This model is fundamental for the solidification and optimization of gyroscope structure.

CHAPTER 1. INTRODUCTION

The first chapter presents an overview of gyroscopes and their applications in a variety of fields, the classification of gyroscopes, and the motivation and objective of this research.

1.1. Gyroscopes and Applications

Angular velocity is a quantity to measure how fast an object rotates concerning an inertial frame of reference [1]. Generally, the unit of angular velocity is radians per second or degree per second. The angular velocity is determined by indirect methods which convert it to measurable quantity, such as electric signal.

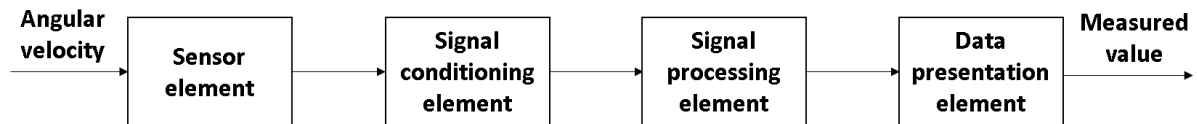


Figure 1-1: Angular velocity measurement system diagram

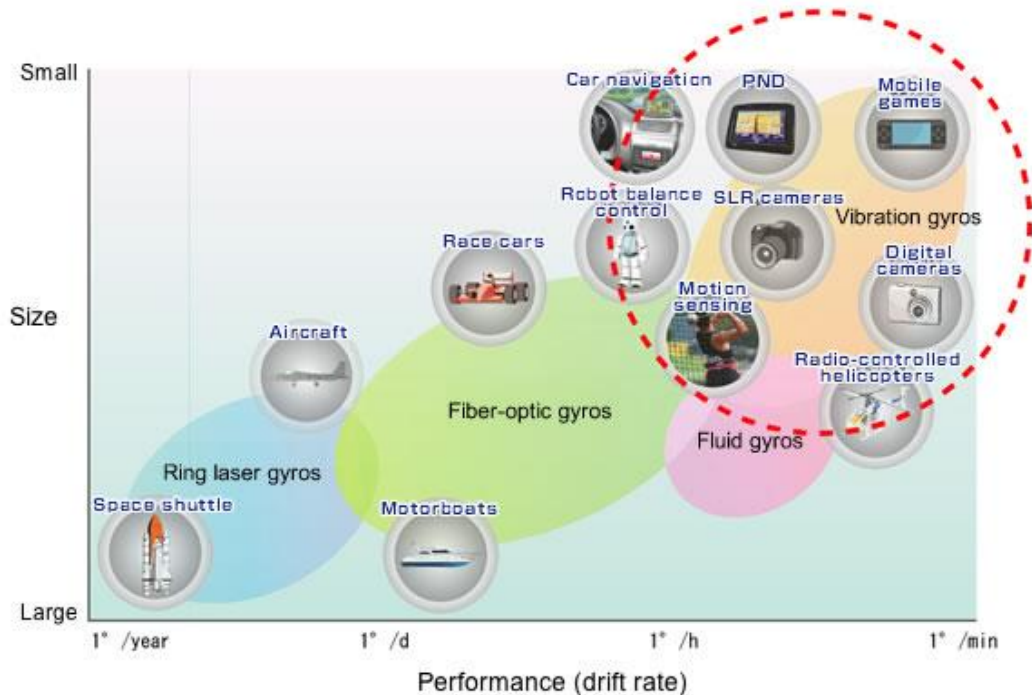


Figure 1-2: Gyroscopes applications [20]

Figure 1-1 shows a diagram of an angular velocity measurement system. The sensor acquires and converts the change of the quantity to be examined to an output response. In some cases, the output response of the sensor is not conveniently calculated, thus signal conditioning is essential in a measurement

system to transform the sensor response to measurable quantity, generally electric signal such as voltage, current, frequency,... The signal processing is used to enhance the output signal of the system, change the output of the signal conditioning element to be more suitable for further presentation. For instance, the analog to digital (ADC) converter transforms analog voltage signal to digital form to be easily calculated and input to the computer. The data presentation element displays measured value to be easily perceived.

Gyroscopes are devices used to sense the rotation rate of an object concerning an inertial frame of reference [2]. Gyroscopes play an important role in a variety of fields [3][4]. Firstly, gyroscopes are applied in automotive applications which can be listed as anti-rollover systems [5], electronic stability control [6][7]. Moreover, gyroscopes are also used in robotics applications [8][9], military applications [10][4] such as navigation [11][12], aeronautics, and astronautics [4]. Some other applications are mobile phone [13], virtual reality[14][15], digital camera [16], motion-sensing [17][18], medical , smart home [19],...

1.2. Classification of Gyroscopes

1.2.1. Mechanical Gyroscopes

The gyroscopes mechanism was presented in 1852 by physicist Léon Foucault [21]. The conventional mechanical gyroscope typically comprises a massive rotor rotating around the spin axis [2]. The more complex design consists of a metal frame and rings around (also called gimbals) for a more accurate device (see Figure 1-3) [22]. The gimbals assisted bring about desired rotational freedom. The number of gimbals refers to the classes of gyroscope: gyroscope with two gimbals called two-degree-of-freedom (the spin axis has two degrees of rotation, gyroscope with three gimbals called three degree-of-freedom [22].

The working principle of these gyroscopes is based on the law of angular momentum conservation which proves that the spinning axis of the rotor tends to remain unchanged unless experienced change in direction [23] (see Figure 1-4). As a result, the spinning rotor tends to resist any changes in its rotations axis. Therefore, when the device rotates with angular rate ω , or experiences a unchanged external torque, gyro precession motion acts on its rotation axis at a constant angular rate [2].

$$C_y = -I\Omega\omega_z \quad (1)$$

$$C_z = I\Omega\omega_y \quad (2)$$

In which C_y and C_z corresponds to torques exerting along y and z axis, I refers to the polar mass moment of spinning mass, Ω is the angular rate of the rotor along spin axis, ω_y and ω_z are precession velocities along y and z axis.

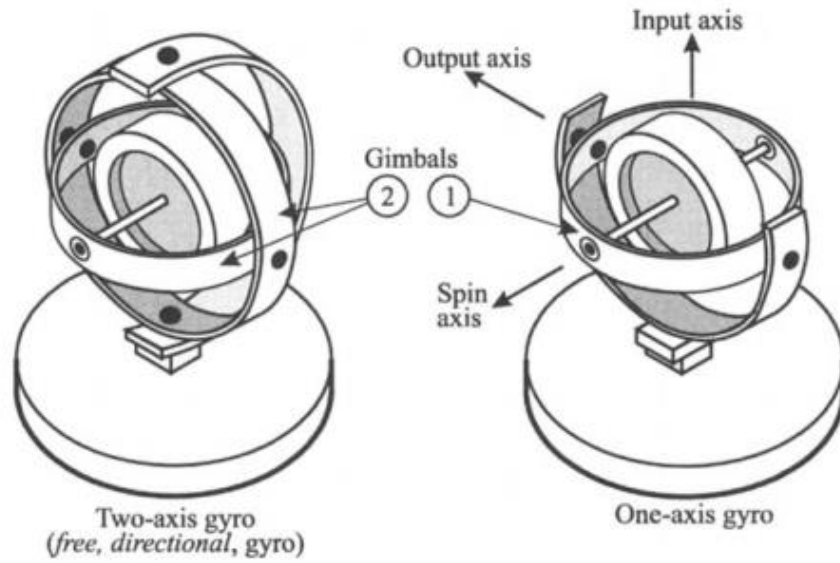


Figure 1-3: Mechanical gyroscopes structure [22]

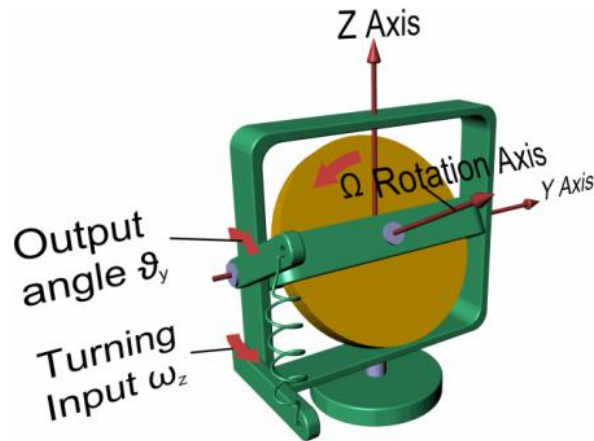


Figure 1-4: Mechanical gyroscopes [2]

A spring system with known stiffness is used to calculate the output angle, making it possible to determine the applied input angular rate [2] (shown in Figure 1-4).

The conventional mechanical gyroscopes encounter several drawbacks which can be listed as large volume (macroscopic gyroscope), low efficiency because of the erosion of rotational coupling, thus reduce the sensor accuracy, expensive [24]

1.2.2. Optical Gyroscopes

The optical gyroscopes working principle is based on the Sagnac effect, which was illustrated by a French physicist, G.Sagnac in 1913 [25]. Sagnac found out that in a closed-loop interferometer, a rotation around the axis of the loop results in different arrival time of two light beams traveling in the opposite direction, thus inducing phase shift between two beams [25][26] (Figure 1-5). The propagation times difference can be calculated using the following equation:

$$\Delta\tau = \frac{4\pi R^2\Omega}{c^2} \quad (3)$$

In which R is the path radius, c relates to light beam velocity, Ω is the rotating rate. With continuous waves of frequency ω , the corresponding phase shift is:

$$\Delta\phi = \omega\Delta\tau = 4\pi R^2\Omega \quad (4)$$

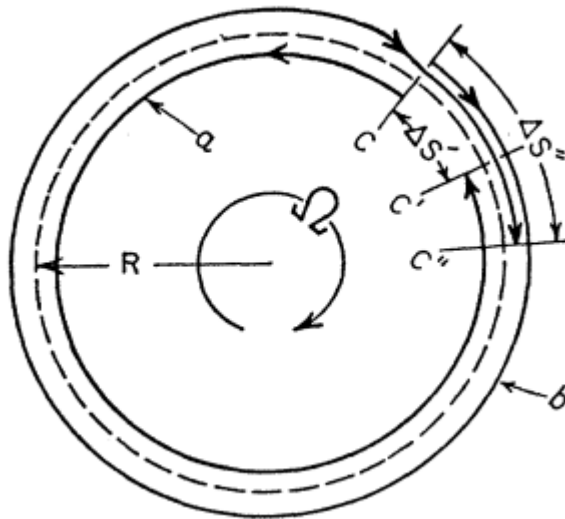


Figure 1-5: Sagnac effects [27]

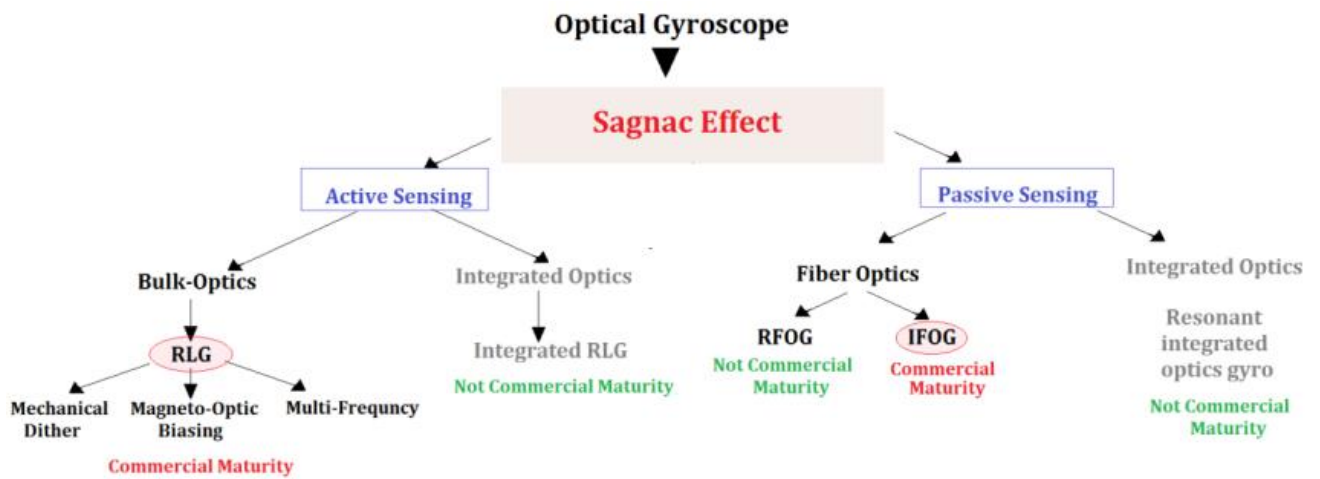


Figure 1-6: Optical gyroscopes classification [2]

The optical gyroscope is classified into active and passive configurations (Figure 1-6). Ring Laser Gyroscopes (RLG) [28][29] and Interferometric Fiber Optic Gyroscopes (IFOG) [30][31] are the most popular gyroscopes technology [2][32]. The ring laser gyroscopes operated based on a ring laser, in which, the rotation rate of cavity is measured by determining frequencies difference of two independent counter-propagating resonant modes over a similar path (Figure 1-7) [33]. These gyroscopes were initially presented by Macek and Davis in the US in 1963 [34].

Generally, a laser ring gyroscope consists of a triangular glass block and several mirrors are set up at each corner to generate a triangular optical resonator. The angular rate can be detected by the change in the resonant frequency of the device or the interference pattern created by the two opposite direction laser beams. The ring laser gyroscopes possess the advantages of no moving part, high accuracy, and compact [33]. However, this gyroscope may experience an effect called the lock-in effect which occurs at a low rotation rate, weak mutual crosstalk between two laser beams leads to standing waves inside the structure [33][35]. Therefore, the device may inconsiderate to low rotation velocity. In recent years, attempts were made to obtain ring laser gyroscope optimization, performance enhancement.

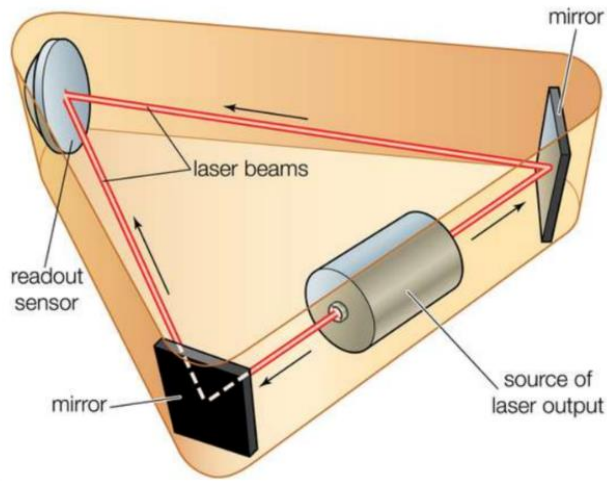


Figure 1-7: Laser ring optical gyroscopes configuration [36]

The Interferometric Fiber Optic Gyroscopes, whose working principle is based on an optical path. These gyroscopes consist of a proper laser source which generates laser light passing through a beam splitter, finally coupling at the ends of a single mode fiber (Figure 1-8). Due to the Sagnac effect, the induced angular rate can be determined by the phase difference of two light beams [37].

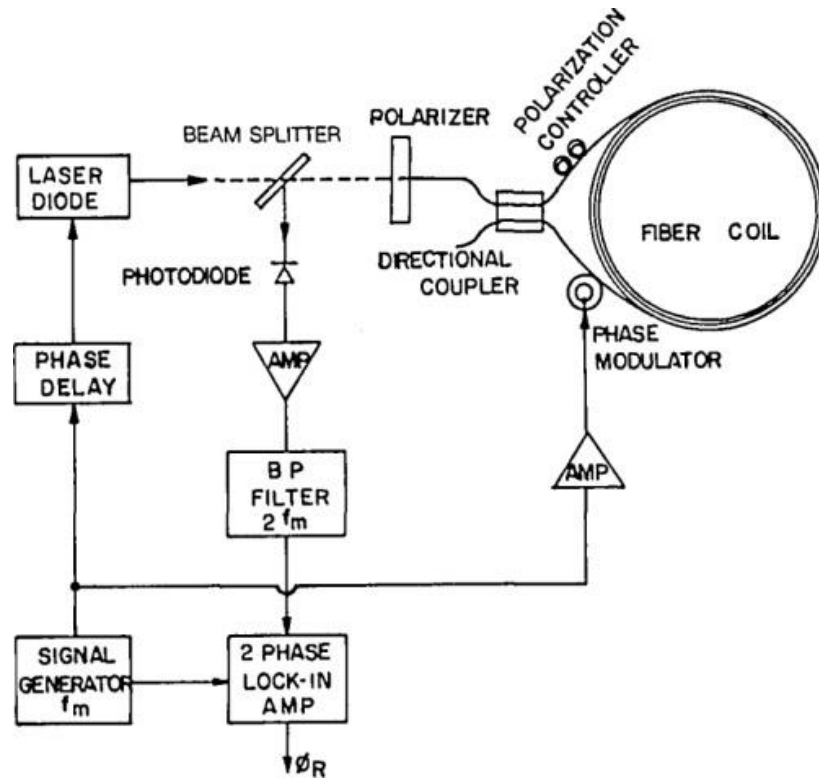


Figure 1-8: Interferometric fiber optic gyroscopes working diagram [38]

1.2.3. Micro-Electro-Mechanical (MEMS) Gyroscopes

MEMS gyroscopes have the advantages of small size, low cost, robust, and low power consumption in comparison to conventional gyroscopes [39]. Therefore, MEMS gyroscopes are commercialized and applied in a variety of

applications including civil and military [10], smartphones, wearable equipment [40], vehicle navigation [41],...

The working principle of MEMS gyroscopes is based on Coriolis acceleration which is described in Figure 1-9 [42]. If a mass moving in direction x with velocity \vec{v} rotates around z axis with angular velocity $\vec{\Omega}_z$, it will experience Coriolis force in the direction which is orthogonal to both driving direction and rotation axis. The Coriolis force is proportional to the applied angular velocity.

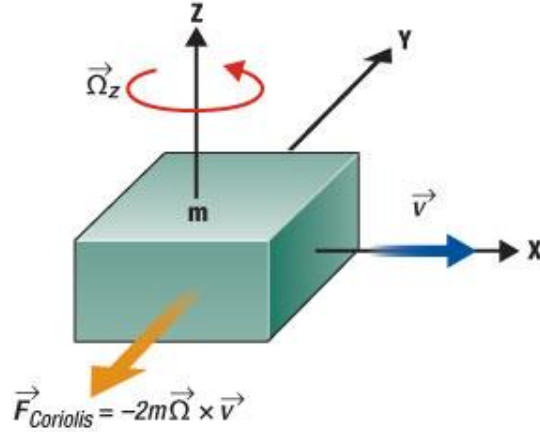


Figure 1-9: Coriolis effect [43]

MEMS Gyroscopes consist of a vibrating proof mass as a sensing element attached to the sensor frame as shown in Figure 1-10. The applied angular rate can be measured by calculating the displacement of the proof mass which corresponds to the acquired signal from the capacitive sensing signal [44].

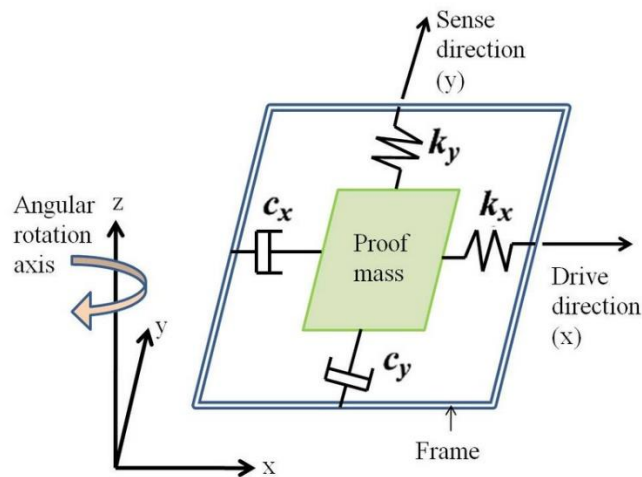


Figure 1-10: MEMS gyroscopes [45]

We have following Equations:

$$m\ddot{y} = -k_y y - c_y \dot{y} + F_{Drive} \quad (5)$$

$$m\ddot{z} = -k_z z - c_z \dot{z} + F_{C_z} \quad (6)$$

$$F_z = |2m\Omega \times v| \quad (7)$$

Where k_y and k_z relate to elastic stiffness parameters proper of the frame, c_x and c_y correspond to damping coefficients.

The development of MEMS gyroscopes attracts much attention from researchers. Recently, in 2017, Pyatishev et al. presented a comb-shaped drive with an extended capacity gradient that obtains a high efficiency performance [46].

1.2.4. Fluid Gyroscopes

The MEMS gyroscopes, with the use of proof mass, may encounter several drawbacks, for example, low shock resistance, fragility, complex manufacturing process [47]. To overcome these disadvantages, fluid gyroscopes use a gas or a liquid as moving and sensing elements. These gyroscopes are generally classified into two types: Jet flow gyroscopes [48][49] and thermal gas gyroscopes [50][51].

The jet flow gyroscopes work based on the Coriolis effect. These gyroscopes are comprised of a jet flow which is created by a pump and two symmetrically placed sensors (thermal sensors) (Figure 1-11) [52]. In case of no rotation, the temperature profile of the two sensors is identical. When the device rotates with an angular rate ω , a Coriolis force acts on the jet flow, leading to the deflection of jet flow. As a result, the temperature profiles of the two sensors are different [52]. The asymmetric temperature distribution can be converted into an electrical signal to determine the rotation rate.

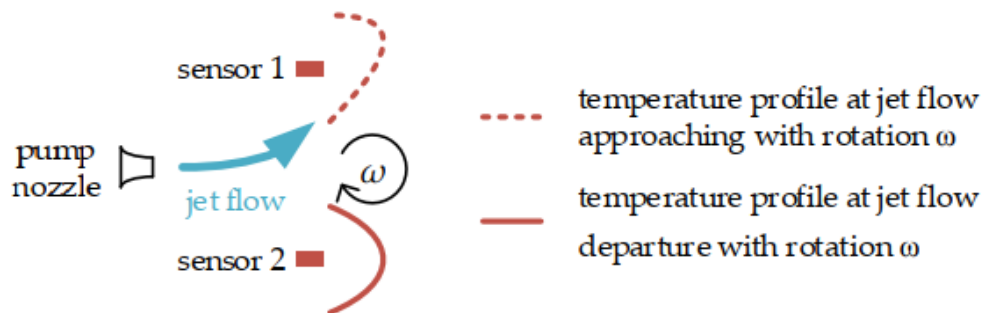


Figure 1-11: Jet flow gyroscopes [52]

In these gyroscopes, the most fundamental factors are the temperature coefficient of resistance which have a considerable effect on the sensitivity of gyroscopes. Besides, the structure of gyroscopes and jet flow velocity must be intensively investigated to optimize the sensor performance.

Jet flow gyroscopes appeared in the 1960s and have been applied in military field. The research group from Ritsumeikan University, Japan has improved a dual-axis jet flow gyroscope which contained a piezoelectric pump and four

thermistors as sensing elements, covered by an aluminum case (Figure 1-12). They optimized the fluid gyroscope by optimizing the design and geometry structure of the sensor and the material of thermistors. As a result, they achieved performance enhancement gyroscopes with a resolution of 0.5°/s and a bandwidth of 65Hz in 2006 [53]. However, the main drawbacks of the mentioned gyroscopes are large dimensions, inaccuracy due to the assembly limitation. To address this problem, the research group from Tsinghua University presented a monolithic jet flow gyroscope using only one chamber with a diaphragm pump to create jet flows [52].

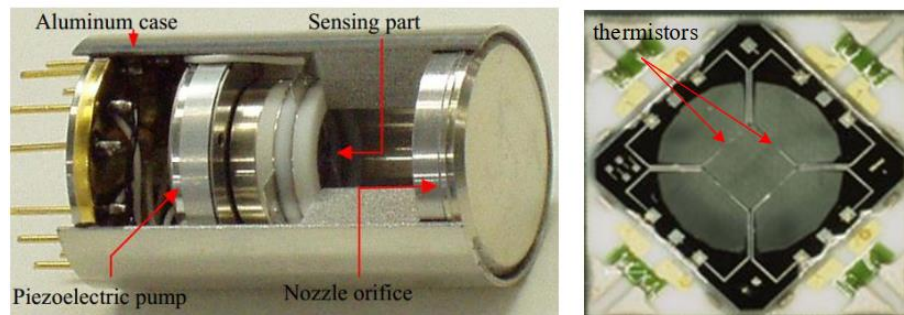


Figure 1-12: Cut view of dual-axis jet flow gyroscope and graph of sensing element [53]

The thermal gyroscopes structure contains a heater and four symmetrical thermistors used as sensing elements as illustrated in Figure 1-13. The heater is warmed up to a high temperature and creates a similar temperature distribution on two sides of the working region. When the sensor experiences an angular rate, due to the Coriolis effect, the thermal flows are deflected, thus the temperature profile is no longer symmetrical. The angular velocity then can be calculated by observing the difference between the two temperature profiles [52].

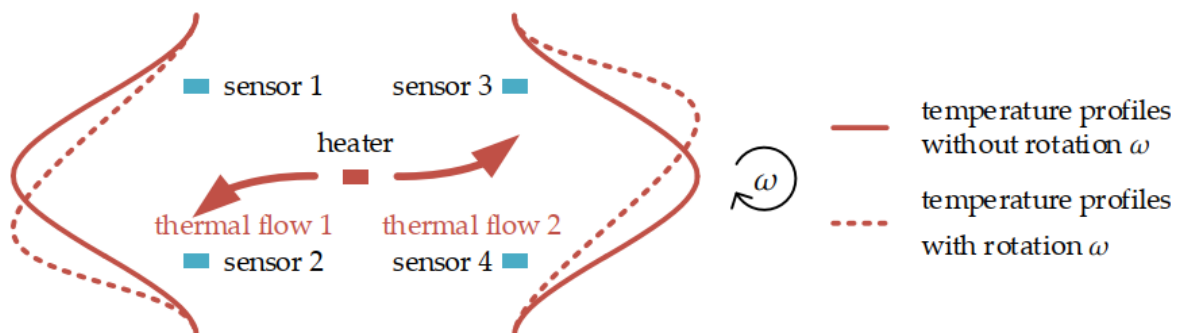


Figure 1-13: Thermal gas gyroscopes [54]

1.3. Contributions and Thesis Overview

With the innovation of technology, mechanical gyroscopes, and optical gyroscopes (ring laser gyroscopes and interferometric fiber optic gyroscopes) obtain high accuracy; however, these mentioned gyroscopes are too expensive and large to apply in some recently popular applications. Especially, optical gyroscopes which are bulky and require optical instruments are not easily integrated into MEMS systems. Due to the advancement of fabrication technology, the MEMS gyroscopes have the advantages of high performance, reasonable price, small size. Nevertheless, MEMS gyroscopes use proof mass as a vibrating element, leading to disadvantages of low shock resistance, fragility. In fabricating MEMS gyroscopes, the resonant frequency of two vibrating modes is one of the most important design factors. The unwanted vibration of mass also results in an undesired signal. To overcome these drawbacks, researchers have designed and improved processing signal circuits. However, this may lead to a complex fabrication process, more expensive devices and instability acquired signals.

In this thesis, a fluid gyroscope based on corona discharge ion wind and thermal convective effect has been presented, modeled, and simulated to measure the angular rate. The gyroscope working principle is extensively studied and analyzed. Multiphysics simulations of fluid gyroscope were conducted using finite element method by COMSOL Multiphysics software for accounting for all relevant fluids, thermal aspect. The simulation results validate the phenomenon considered and show a good agreement with the experimental results of our research group. The numerical study is a fundamental and useful approach for the verification and optimization of the sensor.

CHAPTER 2. DESIGN AND PRINCIPLE OF PROPOSED GAS GYROSCOPE

2.1. Corona Discharge Ionic Wind

Figure 2-1 shows the I-V characteristics of a glow discharge. The voltage is a nonlinear function of electric current. The characteristics consist of three regimes: dark discharge, glow discharge, and arc discharge [55]. The corona discharge appears in dark discharge or Townsend regime, just before glow discharge regime.

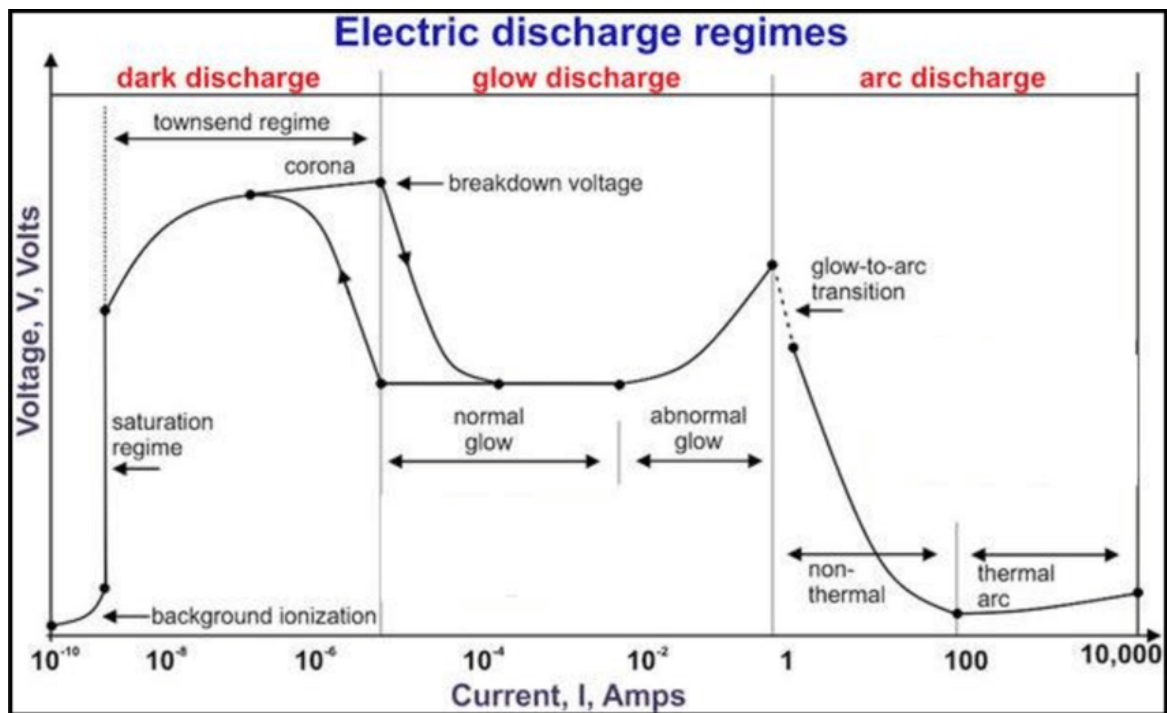


Figure 2-1: I-V Characteristics of glow discharge [55]

The ionic wind was investigated in 1899 by Chattock [56], but have known even before and become popular with the research of Robinson which stated the capability of corona discharges to perfect blowers in the appearance of any moving mechanical part in 1961[57]. When a sufficiently high voltage is applied between two electrodes in atmospheric air, if the electric field is sharply non-uniform (point-to-plane, wire-to-plane,... configuration), corona discharge is generated [58][59]. The air around the sharp tip electrode is ionized. Because of the electric field, the Coulomb force exerts on these ions, leading to the movement of ions from active electrodes to the grounded electrode. These total Coulomb forces are also known as electrohydrodynamics forces. The ions move inside space between two electrodes and many collisions between moving ions and

neutralized air molecules occur, leading to momentum transfer, forming a gas flow, which is called “ionic wind”(Figure 2-2) [60].

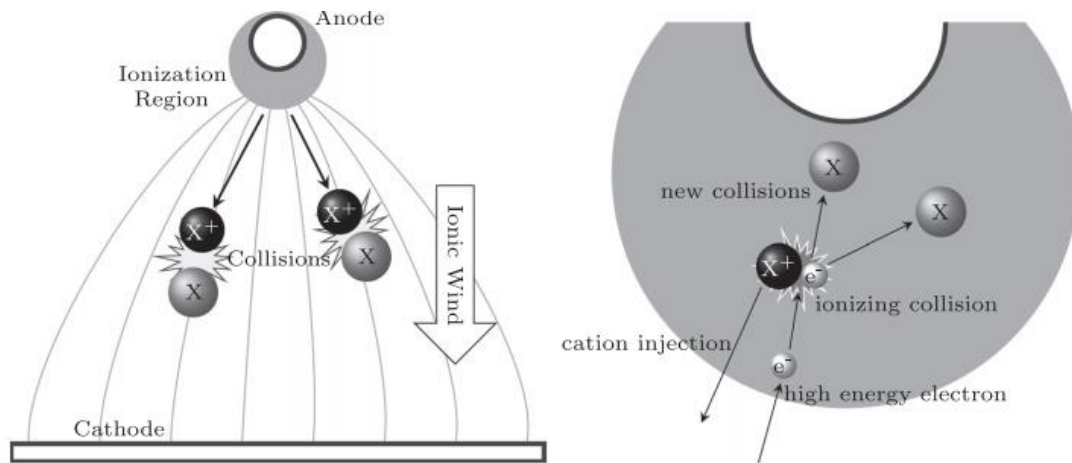


Figure 2-2: Corona induced ionic wind principle [60]

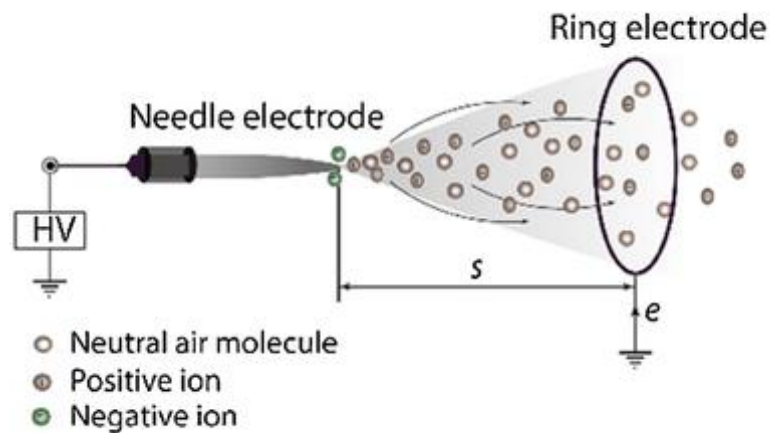


Figure 2-3: Needle-to-ring configuration [61]

The ion wind has attracted tremendous attention from researchers. The publications of Matthew Rickard et al. in 2005 presented that when an electric field is generated between a high voltage induced sharp object and a grounded electrode, air surrounding the electrodes move and the ionic wind created by corona discharge flows from a sharp nozzle to a grounded plane with velocity up to approximately 10 m/s. When flowing between two electrodes, ions collides and transfers momentum to other neutral air molecules. The characteristics of the ionic wind have been examined [58].

Moreau et al. generated ionic wind in a tube or on a plate surface. The corona ionic wind velocity was up to 25 m/s and its influence on airflow was observed and investigated [60][62][63].

Several research groups examined the numerical studies of the corona discharge effect. Cagnoni et al. used a staggered solution algorithm to resolve the partial differential equations of electrohydrodynamics flow, approaching corona ion wind estimation [60].

The different configurations to generate ionic wind have been presented. However, the most popular configurations are needle-to-plate [64] or needle-to-ring configurations [65].

Despite the complexity of the nature physics of corona discharge, the implementation of ionic wind generation is not difficult. With the advantages of self-sustained, small size, low weight, moving part elimination, simple operation, the ion wind is applied in a variety of fields in commercial and industrial. For example, they are utilized in photocopy devices, ozone production [66], pollutants removal from emission [67], surface treatment [68], thrust production [69], unwanted electron removal in airplane surfaces, ... Moreover, corona discharge ionic wind is applied in different types of sensors such as MEMS sensors, pressure sensors [70], inertial sensors [71],...

2.2. Coriolis Effect

The proposed fluid gyroscope working principle is based on Coriolis force which is illustrated in Figure 17. The Coriolis effect was presented in the 19th century by a French engineer-mathematician Gustave-Gaspard Coriolis in 1835. When an object moves in a rotating frame of reference, an inertial accelerometer, known as the Coriolis accelerometer acts on an object, leading to the appearance of inertial Coriolis force, resulting in the deflection of the object moving direction. The Coriolis force exerts to the right of moving direction in case of counterclockwise rotation of reference frame or to the left in case of clockwise rotation.

Consider $\vec{\omega}$ is the angular rate of the rotating frame, \vec{v} corresponds to the velocity of the object. The Coriolis accelerometer can be calculated as:

$$\vec{a}_c = 2 \times \vec{\omega} \times \vec{v} \quad (8)$$

The Coriolis force is:

$$\vec{F}_c = 2 \times m \times \vec{\omega} \times \vec{v} \quad (9)$$

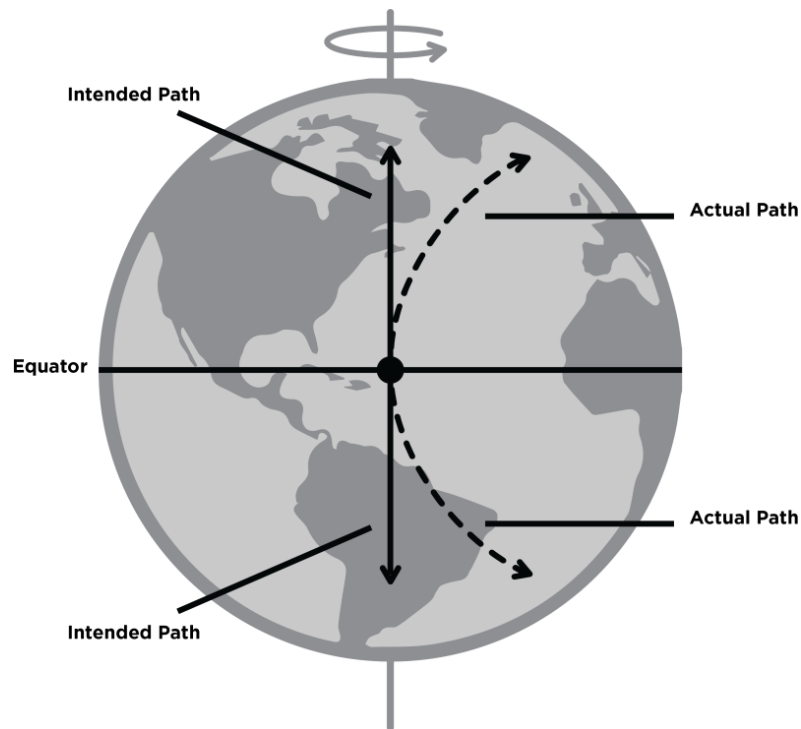


Figure 2-4: Coriolis effect [79]

2.3. Thermal Convection

Heat transfer is a mechanism of thermal energy transfer between two physical systems. Heat transfer contains different mechanisms: thermal conduction, thermal convection, thermal radiation.

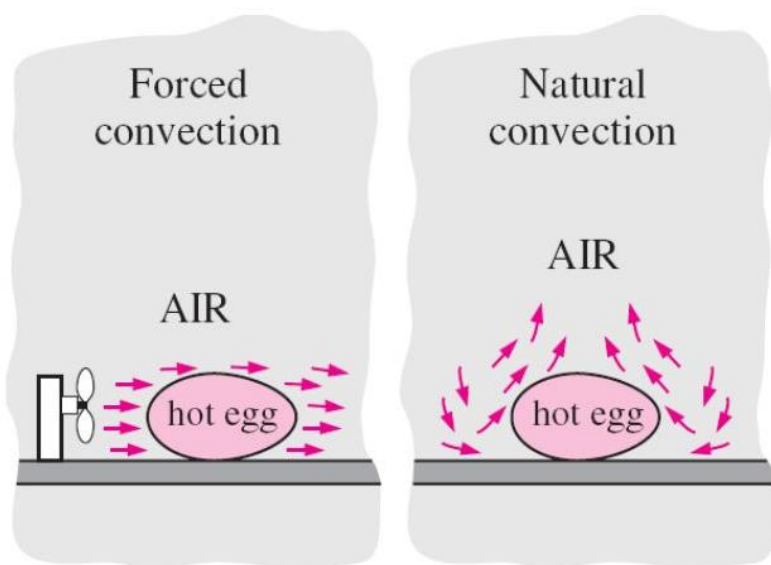


Figure 2-5: Forced convection and natural convection [81]

Thermal convection is the heat transfer between an object and its surrounding environment when the temperature of the object differs from the surrounding fluid. This effect contains molecular diffusion and fluid movement by means of force (forced convection) or free (natural convection) (see Figure 2-5).

The heat flux can be determined by Newton's law:

$$q = hA\Delta T \quad (10)$$

Where q is convective heat on the surface, A relates to the cross-section of boundary surface, h corresponds to heat transfer coefficient, ΔT is the temperature difference.

2.4. Bridge Measurement Circuit

A thermistor is a thermal resistor whose resistance depends on temperature. The thermistor is classified into Negative temperature coefficient (NTC) and Positive temperature coefficient (PTC). When using NTC, an increase in temperature leading to a decrease in resistance. In contrast, with PTC, an increase in temperature resulting in increase of resistance (Figure 2-6).

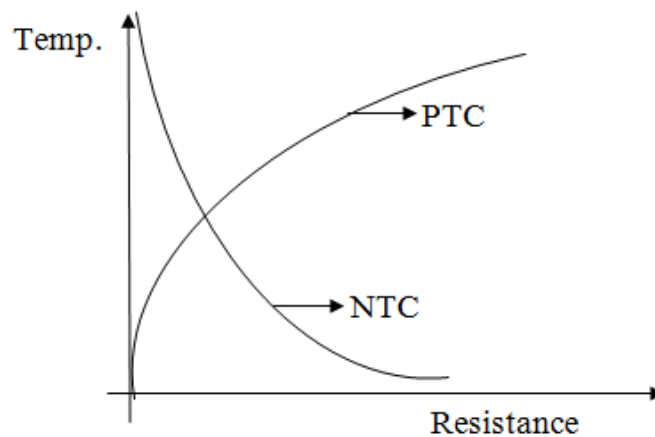


Figure 2-6: Thermistor temperature characteristics curve [80]

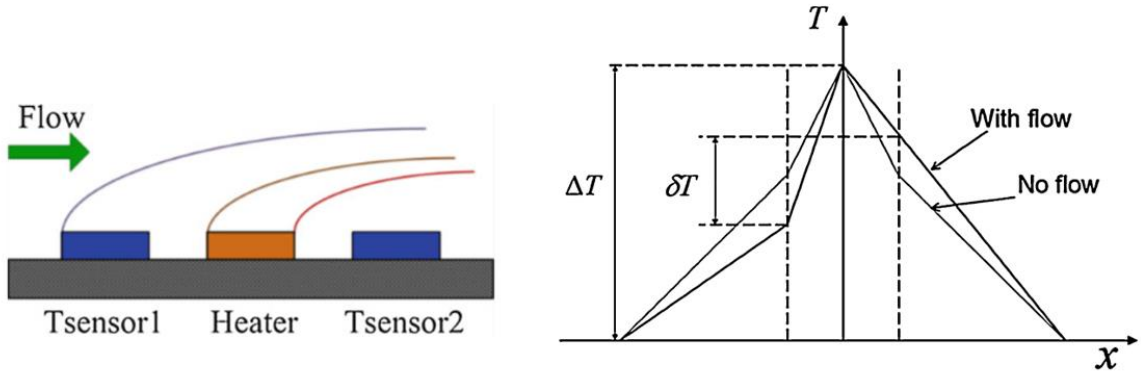


Figure 2-7: Wind sensor based thermal resistors schematic and temperature distribution of sensor [72]

Thermal resistors are applied in a variety of fields, especially in wind sensors. The wind sensor based on the thermal resistors schematic is shown in Figure 2-7. The hotwire (thermistor) is warmed up by applying an electric current due to the Joule effect. When wind flows through the hot wire, the hot wire temperature reduces. The heat brought by the wind follows the Equation:

$$P = (A + BU^{0.5})\Delta T \quad (11)$$

In which P is the heat taken away by the wind, U corresponds to wind velocity, ΔT is the temperature difference between the hot wire and surrounding environment, A and B are parameters depending on the fluid property and sensor dimension.

The wind sensor contains two temperature sensors which can be thermal resistors placed on two opposite sides of the heater. The wind velocity can be calculated by temperature difference measurement as illustrated in Figure 2-7.

The hot wire with extremely small size (diameter approximately several micrometers) can be used to measure the flow velocity and have almost no influence on the flow. Besides, the thermistor has advantages of high sensitivity, immediate responses to temperature change.

Figure 2-8 shows the Wheatstone Bridge Circuit to measure the output signal. The bridge circuit which is used to measure unknown resistance consists of four resistances.

The output of the circuit can be calculated:

$$V_{out} = \left(\frac{R_1}{R_1 + R_2} - \frac{R_3}{R_3 + R_4} \right) V_{in} \quad (12)$$

The circuit is a null or balanced condition when

$$\frac{R_1}{R_2} = \frac{R_3}{R_4} \quad (13)$$

The dependence of output voltage on the change of resistance R_4 (sensitivity of bridge circuit) can be expressed by:

$$\frac{\Delta V_{out}}{\Delta R_4} = \frac{R_3}{(R_3 + R_4)^2} V_{in} \quad (14)$$

The whole sensitivity of the bridge circuit is:

$$\frac{\Delta V_{out}}{V_{in}} = \frac{R_2 \Delta R_1 - R_1 \Delta R_2}{(R_1 + R_2)^2} - \frac{R_4 \Delta R_3 - R_3 \Delta R_4}{(R_3 + R_4)^2} \quad (15)$$

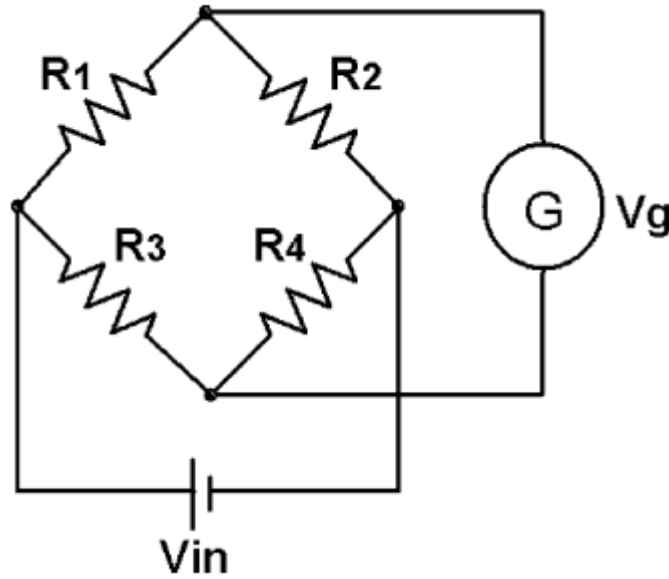


Figure 2-8: Wheatstone bridge circuit [73]

2.5. Gas Gyroscopes Working Principle

The gyroscope working principle is described in Figure 2-9. The gas gyroscope structure consists of two primary chambers: the jet flow generation chamber and the working chamber. In this work, the jet flow is created by the corona effect. It is due to advantages of corona discharge ionic wind such as stability, easy integration, no moving parts requirement, no impoverishment. A sufficiently high voltage is applied between pin-ring configuration electrodes, leading to the generation of an ionic wind. A pin acts as an ion emission electrode, a ring served as a grounded electrode. The average velocity of ionic wind can be determined by the following Equation:

$$U = k\sqrt{I/\rho\mu} \quad [57] \quad (16)$$

In which $\mu = 1.6 \times 10^{-4} m^2 V^{-1} s^{-1}$ is the ion mobility, $\rho = 1.2041 kg.m^{-3}$ is air density, I corresponds to current which around several

μm , k is a parameter which depends on distance and environment between electrodes.

The higher current, the faster the ion wind. Thus, to increase the velocity of flow, applied voltage between two electrodes needs to become higher to increase current. However, if the applied voltage is too high, the system may become instability.

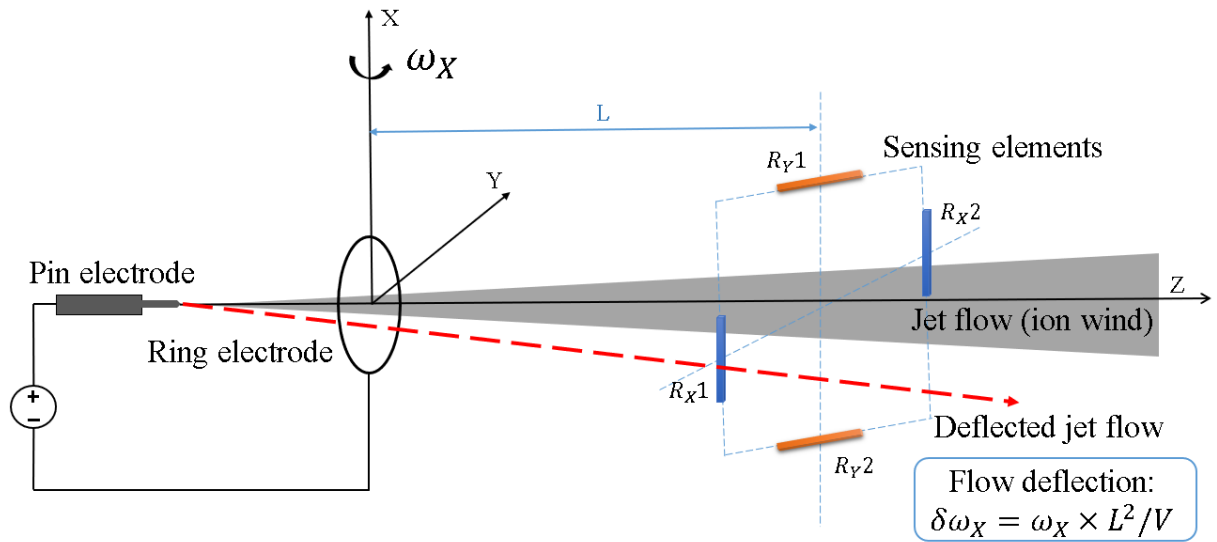


Figure 2-9: Gas gyroscope working principle

The ionic wind is guided directly to the working chamber. In the working chamber, four hot wires are placed downstream and symmetrically to sense the angular velocity change of the device. The four hot wires are heated by an electric current. Without rotation, ionic wind flows straight into the middle of the working chamber. The temperature distribution is symmetric between four thermistors. In contrast, when an angular rate is applied, due to the Coriolis effect, the jet flow is deflected. As a result, the influence of the ionic wind on the symmetric hot wires is different, thus the temperature distribution inside the working chamber is no longer symmetric. The change in temperature of hot wires can be observed by the change in their resistance, which is then converted to an electric signal and measured by a circuit.

The principle of the presented gyroscope is investigated by simulation approach using finite element method (FEM). The FEM technique and procedure are illustrated in the following Chapter. Chapter 3 also refers to simulation study which contains numerical model, simulation model, and boundary conditions.

CHAPTER 3. SIMULATION STUDY

3.1. Finite Element Method

The Finite Element Method (FEM) was firstly introduced by Clough in the early 1960s [74]. To extensively understand the natural phenomena and predict the physics phenomena that happen in the time domain and space domain of a design, researchers can mathematically model and numerically express by partial differential equations (PDEs). For example, conservations laws such as the law of conservation of energy, conservation of mass, conservation of momentum can be demonstrated by PDEs. However, it is difficult to resolve most of these PDEs by analytical methods. Therefore, an approximation of these PDEs is used by discretizations. The FEM is a procedure applied to discrete, approximate, and solve these equations. FEM emerged as a powerful tool for multiphysics problems, especially in fluidics, mechanics, structural [75].

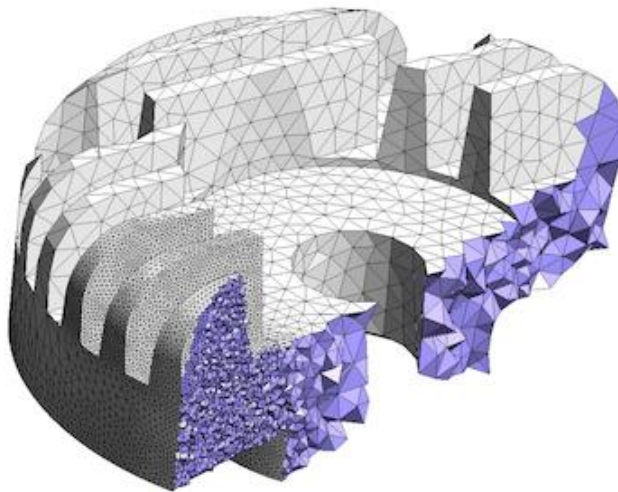


Figure 3-1: A three-dimensional finite element mesh generator [78]

FEM starts with the determination of PDEs describing the physical phenomenon. Then the PDEs are expressed in weak formulation by taking integral of both sides to increase the differential order.

The second step is discretization. The discretization is the division of domain to be analyzed into a finite number of points known as “nodes” and subdomains corresponding to “elements”. Node is the corner point of each element. The group of these non-overlapping elements and nodes is defined as mesh, the act of contributing mesh is call meshing. Then, the local approximate

solutions are assigned to each subspace. The approximate solution is a linear combination of basic functions be included in subspace.

After meshing and setting up boundary conditions, the whole system equation is expressed by a matrix equation. The calculation of the system algebraic equations results in the estimation of actual PDEs solution. If the mesh is finer, the approximated solution is more accurate. Figure 3-1 shows the most popular two dimension and three dimension elements. Triangular elements are mostly used in the simulation. Rectangular elements are usually utilized in structural mechanics analyses or boundary layer meshing.

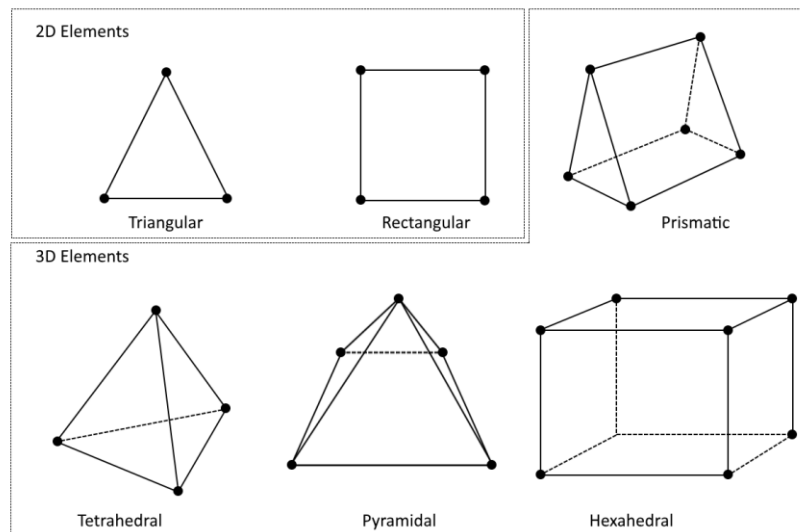


Figure 3-2: Node geometry for two dimensions and three dimension elements [78]

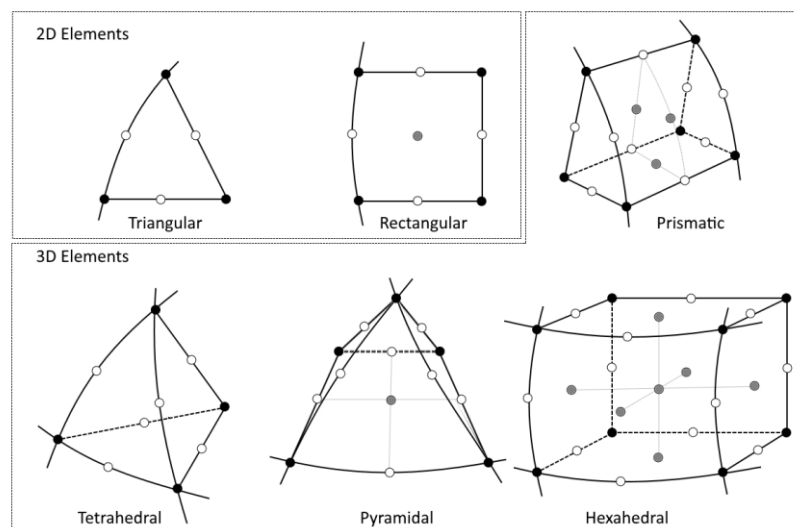


Figure 3-3: Second-order elements [78]

Finally, the complex outputs of FEM are displayed in a format to be understood which can be listed as color fringe, color isocontour, flat shade, slice

model, isosurface, vector plots, streamlines, ...[76] Figure 3-4 illustrates the mesh adaption and simulation results of a droplet movement from an inkjet using COMSOL Multiphysics software.

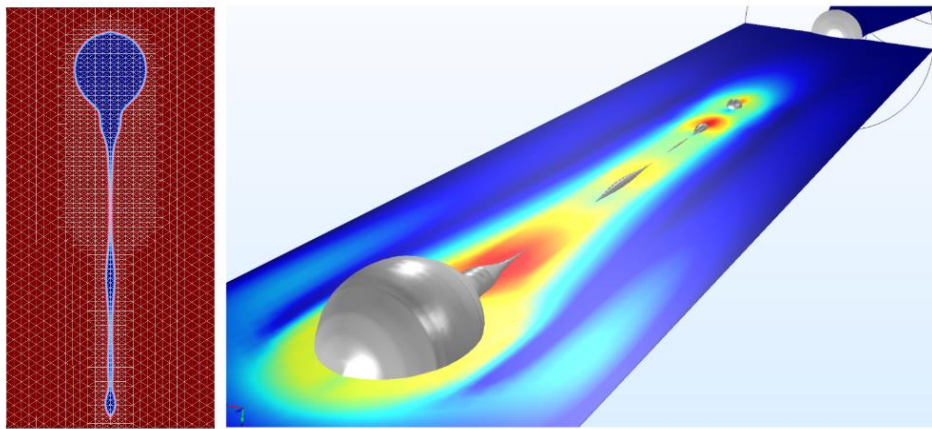


Figure 3-4: Mesh adaption to the droplet movement [78]

3.2. COMSOL Multiphysics Software

COMSOL Multiphysics Software is a finite element analysis platform, providing us an interface and environment for modeling and simulation of physics phenomena toward engineering applications. This software can be applied in multiphysics simulation, such as electromagnetics, structural mechanics, acoustics, fluidics, heat transfer, chemical engineering. COMSOL Multiphysics is used to model, simulate and predict the working processes and natural phenomenon in a variety of fields, helping engineers and researchers to understand the natural physics behind operation devices, optimize the design and avoid errors in manufacturing.

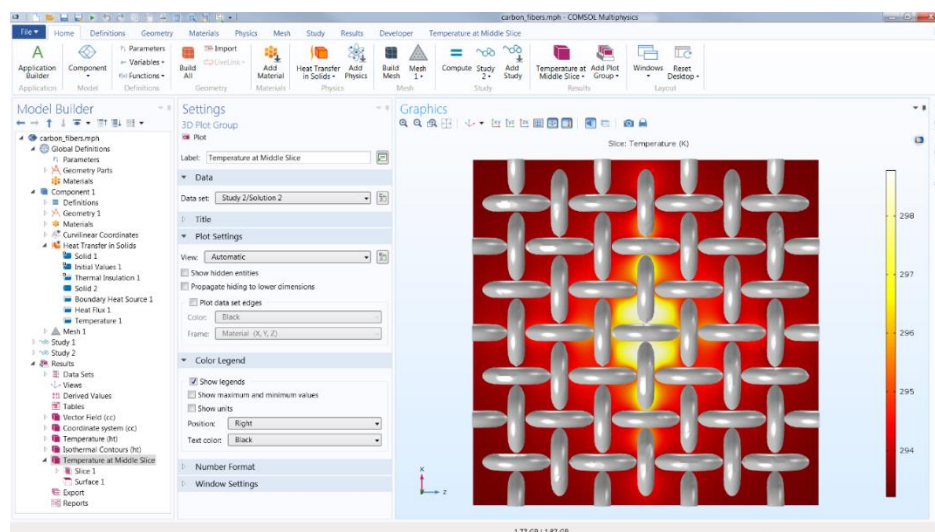


Figure 3-5: COMSOL Multiphysics software user interface [78]

COMSOL Multiphysics compacts all FEM steps in a modeling workflow: building device geometry first, material properties defining, physics selection, resolving boundary conditions, postprocessing for reliable results. This simulation software provides multiphysics analyses, a variety of material library, flexible and adaptive meshing, robust solvers to calculate problems more speedily and trustworthy, plenty of post-processing techniques. COMSOL Multiphysics software has an easy-to-use user interface (Figure 3-5).

3.3. Simulation Model

In this work, the simulations were carried out in three-dimensional (3D) geometry.

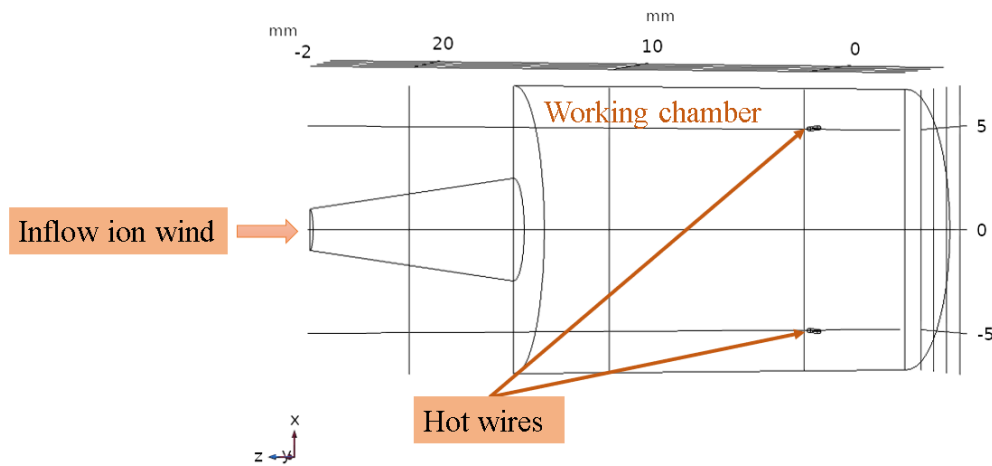


Figure 3-6: Simulation model

The simulation model is shown in Figure 3-6. The simulation model consists of a nozzle in which the ionic wind is guided and flowed straight into the working chamber. The two hot wires are placed symmetrically downstream of the working chamber. The working chamber dimension is 14mm diameter and 20mm length. The hot wires are 0.1mm diameter and 3.5mm length, placed 15mm from the nozzle.

3.4. Numerical Model

The gyroscopes working principle is illustrated by a multiphysics simulation in which the movement of ion wind is described by Navier-Stokes equations for laminar flow and the thermal influence of ionic wind on two hot wires is tracked by Fourier's law of heat conduction.

The Navier-Stokes equations are fundamental partial differential equations for illustrating the conservation of mass, conservation of momentum, conservation of energy; governing the movement of the fluid. These equations which were coined

by Navier, Poisson, Saint-Venant, and Stokes in the early 1800s are known as Newton's 2nd law of motion. The Navier-Stokes equations can be expressed:

$$\rho \left(\frac{\partial \mathbf{u}}{\partial t} + \mathbf{u} \cdot \nabla \mathbf{u} \right) = -\nabla p + \nabla \cdot \left(\mu (\nabla \mathbf{u} + (\nabla \mathbf{u})^T) - \frac{2}{3} \mu (\nabla \cdot \mathbf{u}) \mathbf{I} \right) + \mathbf{F} \quad (17)$$

Where \mathbf{u} corresponds to fluid velocity, p is the fluid pressure, μ is fluid viscosity, ρ is the fluid density. The left-hand term corresponds to inertial forces. The right-hand term is the combination of pressure gradient, internal stress forces, and external forces such as gravity, electric forces,...

The average velocity of ion wind is estimated based on the discharge current as $U = k \sqrt{I/\rho\mu}$ where $\mu = 1.6 \times 10^{-4} \text{ m}^2 \cdot \text{V}^{-1} \cdot \text{s}^{-1}$ is the ion mobility, $\rho = 1.2041 \text{ kg} \cdot \text{m}^3$ the air density, I the discharge current in μA , and k a coefficient and depends on the electrode discharge area and the inter-electrode distance.

When the device rotates with angular rate ω_X , due to Coriolis effect, Coriolis acceleration \vec{a}_{ω_X} is generated, which is calculated by:

$$\vec{a}_{\omega_X} = 2\vec{\omega}_X \times \vec{V} \quad (18)$$

Where \vec{V} is flow velocity vector, $\vec{\omega}_X$ corresponds to angular rate around X-axis.

The ionic wind flow velocity in the deflected direction \vec{V}_{ω_X} is expressed by the equation:

$$\vec{V}_{\omega_X} = \int \vec{a}_{\omega_X} dt = \int 2\vec{\omega}_X \times \vec{V} dt \quad (19)$$

The flow deflection $\vec{\delta}_X$ is:

$$\vec{\delta}_X = \iint \vec{a}_{\omega_X} dt = \iint 2\vec{\omega}_X \times \vec{V} dt \quad (20)$$

The Coriolis force is:

$$\vec{F}_{Coriolis} = 2m(\vec{\omega}_X \times \vec{V}) \quad (21)$$

V is the velocity, which is calculated by:

$$V = \frac{L}{t} \quad (22)$$

L is the distance between ring electrodes and the plane containing hot wires, t is the ionic flow traveling time. Therefore, the deflection of airflow in the working chamber from the normal direction is:

$$\delta_X = \omega_X \frac{L^2}{V} \quad (23)$$

Likewise, if the gyroscopes rotate around Y-axis with angular rate ω_Y , the gas flow deflection is:

$$\delta_Y = \omega_Y \frac{L^2}{V} \quad (24)$$

The more deflected of ionic wind, the more temperature difference between two hot wires. As a result, the obtained voltage is higher.

If the device is simultaneously affected by three components of angular rate around X-axis, Y-axis, Z-axis. The Coriolis acceleration is expressed as:

$$a_X = 2[\omega_Z V_{\omega_X} - \omega_Y V_Z] = 2[\omega_Z(2\omega_X V_Z \times t_L) - \omega_Y V_Z] \quad (25)$$

$$a_Y = 2[\omega_X V_Z - \omega_Z V_{\omega_Y}] = 2[\omega_X V_Z - \omega_Z(2\omega_Y V_Z \times t_L)] \quad (26)$$

In which a_X and a_Y correspond to Coriolis accelerations around X-axis and Y-axis. V_Z is flow velocity around the Z-axis of the sensor.

The flow deflection from the normal axis δ_X and δ_Y is the double integration of Coriolis acceleration. We have:

$$\delta_X = -\frac{\omega_Y L^2}{V} + \frac{2}{3} \omega_X \omega_Z \frac{L^3}{V^2} \quad (27)$$

$$\delta_Y = \frac{\omega_X L^2}{V} - \frac{2}{3} \omega_Y \omega_Z \frac{L^3}{V^2} \quad (28)$$

It can be seen that the second term of the above equations is the influence of the other two axes on the remaining axis, which is known as cross-sensitivity of the gyroscope. When no rotation applied on Z-axis or flow axis, $\omega_Z = 0$, the cross-sensitivity is removed. In other words, the gyroscope can determine two components of the angular rate at the same time.

The thermistor is heated by an electric current. The heat of hot wires is transferred through several mechanisms: conduction, convection, radiation. In this case, the temperature of hot wires is not much high, the thermal radiation is ignored.

For heat convection, Fourier's law states that:

$$q = -k\Delta T \quad (29)$$

Where q is convective heat flux, k is thermal conductivity, ΔT is temperature different.

The ion wind flows through the hot wires, leading to thermal convection. This is classified into forced convection. The convection coefficient is then defined as:

$$Nu = 1.1C \left(\frac{Vd}{v} \right)^n Pr^{0.31} \quad (30)$$

$$h = Nu \frac{\lambda}{d} \quad (31)$$

where C and n are empirical constants, Pr is Prandtl number calculated by $\frac{c_p \mu}{h}$, h is the convective coefficient, d is thermistor diameter, v is the kinematic

viscosity, μ is the viscosity, λ is thermal conductivity, and c_p is the specific heat of gas flow.

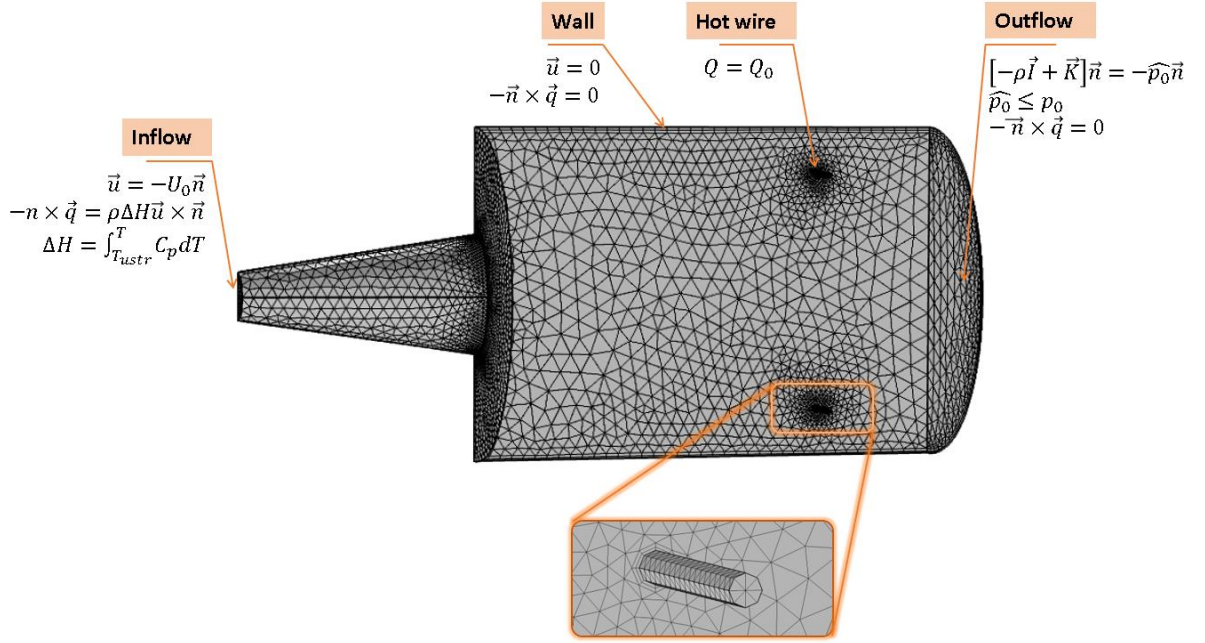


Figure 3-7: Meshing model and boundary condition

The simulations were conducted for the cases the investigated device rotates around X-axis. The angular rate is varied from 0 %/s to 450 %/s. The ionic wind is introduced to the working chamber at a velocity of 4 m/s. The hot wires are heated by an electric current and the heat rate of thermistors is 40 mW. By using this meshing model and boundary condition, the results are illustrated in the following chapter.

CHAPTER 4. RESULTS AND DISCUSSION

In the previous chapter, the numerical study, simulation model, and conditions are presented. This chapter shows the simulation results, discussion, and comparison with the experimental investigation.

4.1. Simulation Results and Discussion

4.1.1. Velocity Profile

The cut view of the velocity contour of the working chamber is illustrated in Figure 4-1. In this work, the ionic wind is injected at a velocity of 4 m/s. In case of no angular rate applied, the ionic wind flows straight into the working chamber. In other cases, when the device rotates, the Coriolis force acts on airflow, leading to the flow deflection. The higher the angular rate, the longer the distance between normal flow direction and deflected airflow.

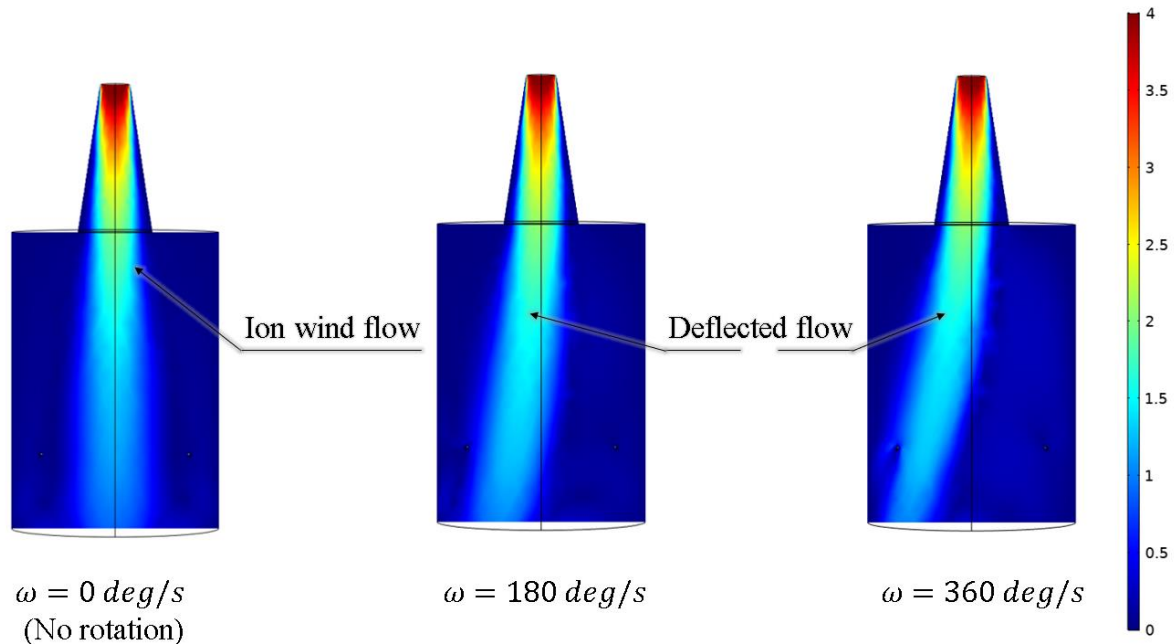


Figure 4-1: Cut view of velocity contour shows the deflection of generated flow at inflow velocity 4 m/s

The value of the velocity at the nozzle is highest and decreases with the increase of distance from the nozzle. The dash blue line and dash green line corresponds to velocity profile in two cases: without and with the applied angular rate of 360 %/s. It is noteworthy that with no applied rotation rate, the velocity profile is symmetrical. In contrast, when the device rotates around X-axis, the jet flow is deflected which is clearly showed by the deflection of velocity profile peak to the left side. This trend is more distinctly at a further distance from the nozzle

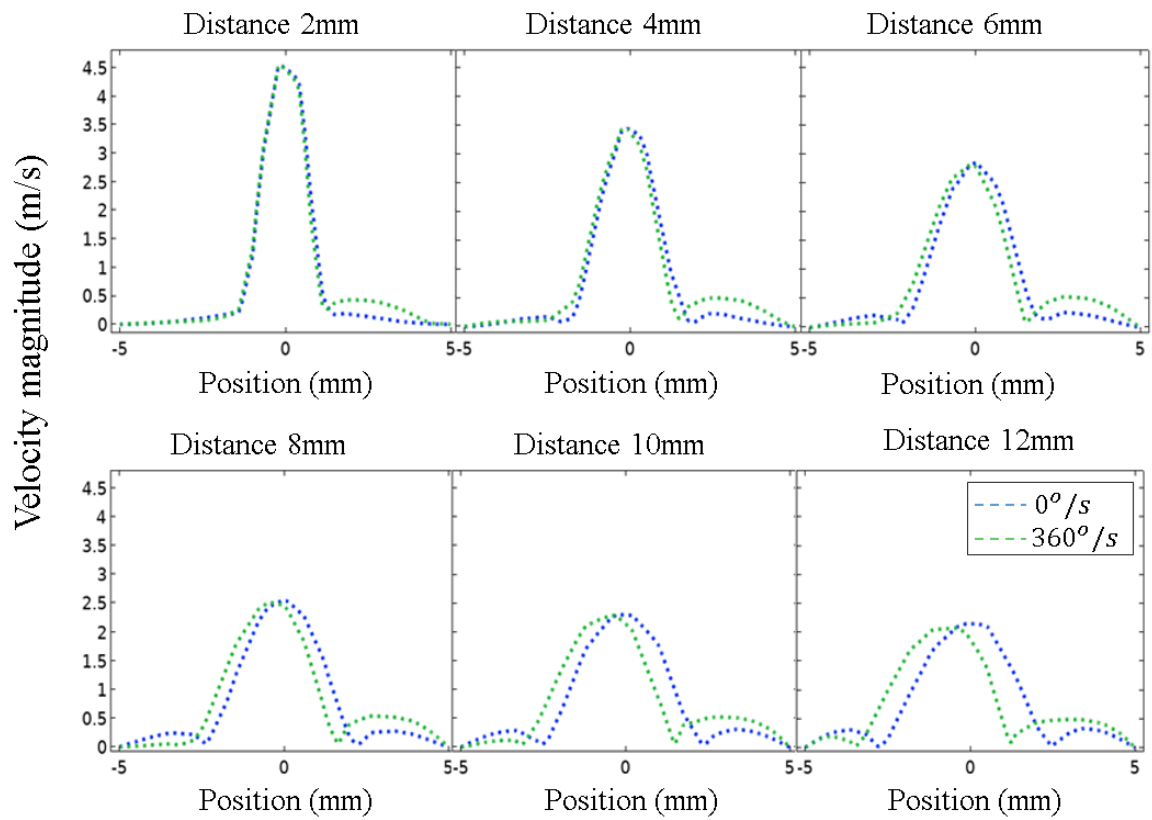


Figure 4-2: Velocity profile in the working chamber at different positions from the nozzle

4.1.2. Temperature Distribution

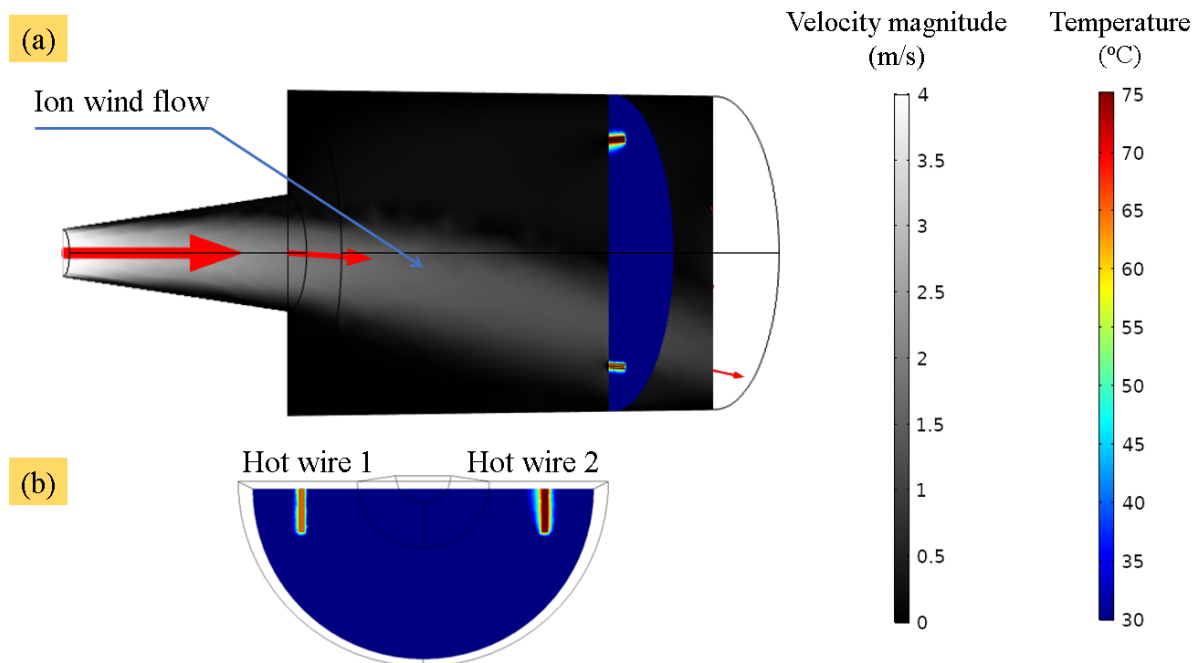


Figure 4-3: Cut view of the velocity field of ion wind (a) and temperature contour on the cross-section of two hot wires in case of angular rate $360^\circ/\text{s}$ (b)

To observe the sensor working principle more obviously, the simulations were conducted with increasing applied angular rate from $0^\circ/\text{s}$ to $450^\circ/\text{s}$. Figure

4-3 illustrates the cut view of temperature contour and velocity field of ionic wind (described by red arrow) with an angular rate of 360 °/s. The ionic wind is deflected to the first hot wire. As a result, the first hot wire is cooled down and has a lower temperature than the remaining. This phenomenon is shown by the cut view of temperature contour in a semi-plane of two hot wires.

For more details, the different temperature between two hot wires is calculated.

$$\Delta T = \frac{1}{V_{hw2}} \int_{V_{hw2}} T dV - \frac{1}{V_{hw1}} \int_{V_{hw1}} T dV \quad (32)$$

Where ΔT is the temperature difference between two hot wires, V_{hw1} , V_{hw2} are volume of first and second hot wire, respectively, T is the temperature of each unit volume.

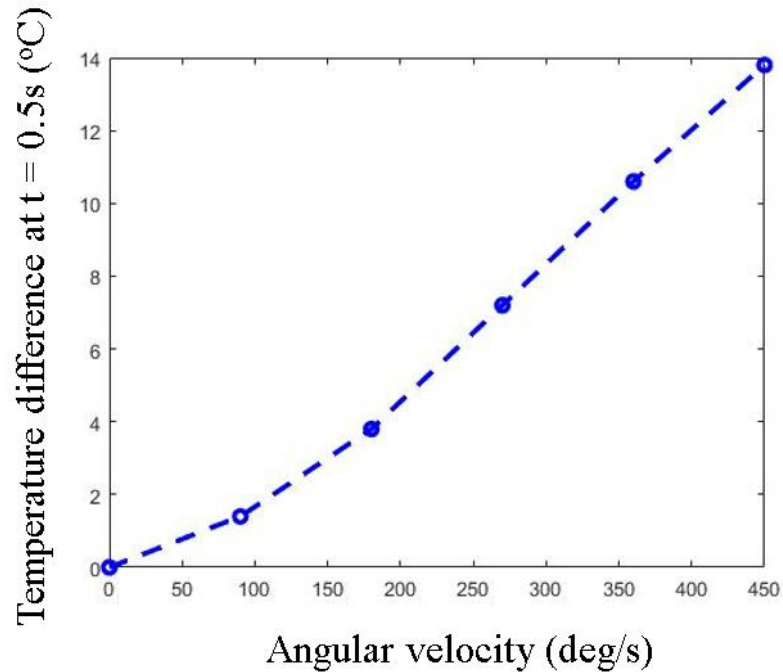


Figure 4-4: The temperature difference between two hot wires at t = 0.5s with angular variation

The increase of temperature difference is associated with the increase of angular rate (Figure 4-4). With an applied angular rate of 450 °/s, the temperature difference reaches 13.8° at t = 0.5s. The sensor has a sensitivity of 0.03 °/deg/s.

The simulation results also show the dependence of temperature difference between two hot wires versus time (Figure 4-5). At first, without the introduction of airflow, the temperature is similar between the two thermistors. After that, the

deflection of airflow leads to a change in temperature distribution. The temperature difference increases versus time and relies on the applied angular rate.

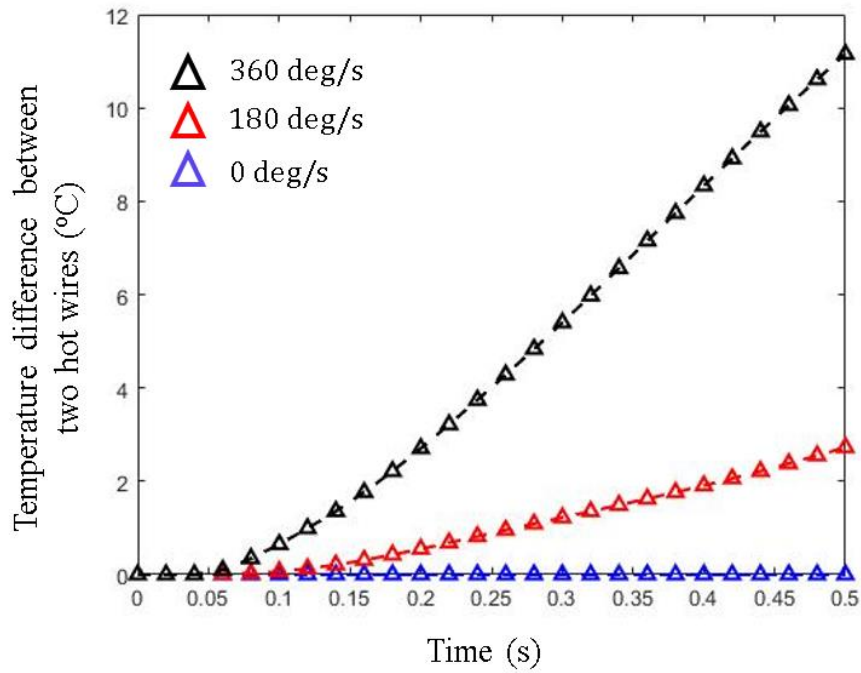


Figure 4-5: Temperature between two hot wires versus time with different angular rate

4.2. Experimental Verification

The experiments were carried out by our research group. Corona discharge ion wind is generated by a pin-ring configuration fabricated by stainless steel SU304. The pin diameter is 0.4 mm and the tip diameter is 160 μm is placed at a proper distance from the ring whose inner diameter is 5 mm, outer diameter is 10 mm and thickness is 0.1 mm. The fabricated gyroscope is shown in Figure 4-6.

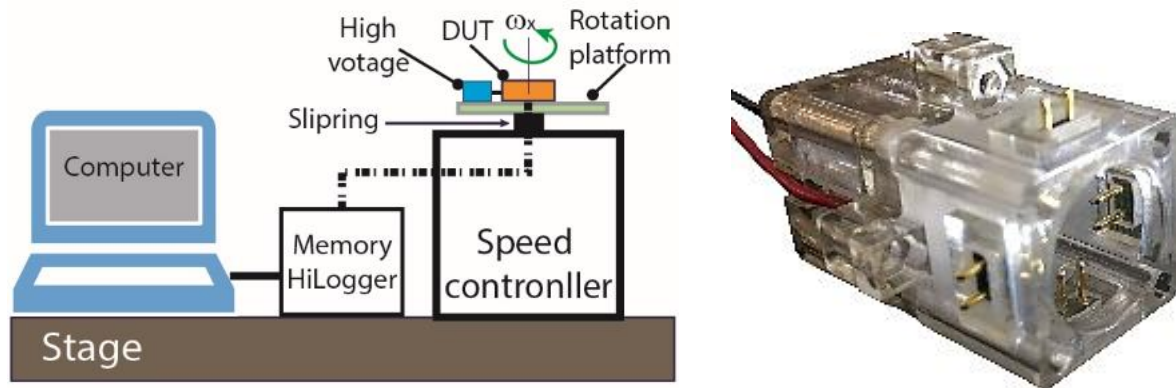


Figure 4-6: Experiment setup and manufactured gyroscope [77]

The experiment setup is illustrated in Figure 4-6. The angular rate is applied on the device through a rotation platform called turntable. The output voltage is measured by an outer bridge circuit. High voltage is generated by EMCO CB 101 and applied to pin-ring electrodes.

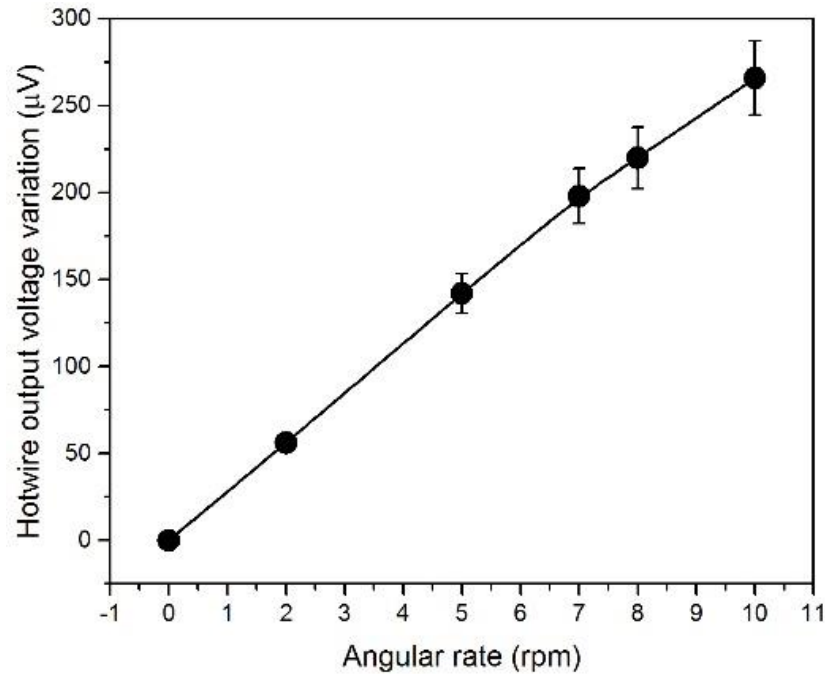


Figure 4-7: Influence of output voltage measured on hot wires on applied angular speed [77]

The measured output voltage versus applied angular rate shows a homologous trend compared to simulation results which illustrate temperature difference between two hot wires with increase angular rate. The estimated sensitivity obtained $4.7 \mu\text{V}/^\circ/\text{s}$. The analytical and numerical approaches show a good agreement with experimental results. This simulation model is a useful tool for confirmation of the working principle of gas gyroscope and optimization of inertial sensor structure for specific applications.

CONCLUSION

This thesis presents a design and working principle of a dual-axis thermal convective gas gyroscope based on corona discharge ion wind. A multiphysics simulation of the model which relates to the behavior of airflow inside the working chamber and the heat transfer between objects is carried out. The analytical and numerical methods are used to simulate the phenomenons and confirm the principle of the gyroscope. The simulation results show the deflection of ion wind due to Coriolis force evidence by velocity profile inside the working chamber and the temperature difference between the two symmetric placed hot wires. To observe sensor principle, simulations are conducted with the variation of rotation rate. The higher the angular rate of the device, the more deviant of jet flow from the intended direction. With an applied angular rate of 450 °/s, the temperature difference obtains 13.8° at 0.5s. The calculated sensitivity of gyroscopes is 0.03 °C/deg/s. The experiments were carried out by our research group and show a good agreement with simulation results.

The presented gyroscope possesses the advantages of robustness owing not to require any vibrating, lower cost and energy consumption inherited from corona discharge approach, tidy and light, and simple operation, no mass production requirement compared with those by other methods. The simulation model can be used to extensively understand the working of the device, analyze the performance efficiency and optimize the sensor design parameter. In the future, there is plenty of room to develop in this research direction. The design of the jet flow gyroscope is improved to be close which means the ion wind is circulated and redistributes the airflow network inside the device. Multiple point-ring electrodes can be used to generate a synthetic jet flow. The geometry parameters of gyroscopes are optimized for efficient performance for specific applications. More experiments are conducted to investigate the working of the device. The gyroscope-based corona discharge and thermal convective effect is a promising tool for low response frequency and flexible design requirement applications, especially ships, ferries,... This jet flow inertial sensor can be integrated into a micro-fluidic, micro-bio, or lab-on-a-chip system.

RELATED PUBLICATIONS

- [1] **Thu-Hang Nguyen**, Ngoc Van Tran, Thien Xuan Dinh, Canh-Dung Tran, Van Thanh Dau, Trinh Duc Chu, Hai Nguyen Hoang, and Tung Thanh Bui, “Numerical study and experimental investigation of an electrohydrodynamic device for inertial sensing”, The 21th International Conference on Solid-State Sensors, Actuators and Microsystems | Transducers 2021. (accepted)
- [2] **Hang Nguyen Thu**, Ngoc Tran Van, Van Dau Thanh, Tung Bui Thanh, Cuong Nguyen Nhu, Trinh Chu Duc and An Nguyen Ngoc, “Study on Thermal Convective Gas Gyroscope based on Corona Discharge Ion Wind and Coriolis Effect”, International Conference on Engineering Research and Applications, Dec. 2020, Lecture Notes in Networks and Systems, vol 178. Springer, Cham.
- [3] Tran Van Ngoc, Dau Thanh Van, **Nguyen Thu Hang**, Chu Duc Trinh, Bui Thanh Tung (2020) Nghiên cứu thiết kế mô phỏng cảm biến vận tốc góc dạng khí hai bậc tự do hoạt động dựa trên hiệu ứng dòng xả corona. Tạp chí nghiên cứu khoa học và công nghệ quân sự, 10. pp. 172-179. ISSN 1859-1403.

REFERENCE

- [1] M. Reze and M. Osajda, *MEMS sensors for automotive vehicle stability control applications*. Woodhead Publishing Limited, 2013.
- [2] V. M. N. Passaro, A. Cuccovillo, L. Vaiani, M. De Carlo, and C. E. Campanella, "Gyroscope technology and applications: A review in the industrial perspective," *Sensors (Switzerland)*, vol. 17, no. 10, 2017, doi: 10.3390/s17102284.
- [3] K. Skopek, M. C. Hershberger, and J. A. Gladysz, "Gyroscopes and the chemical literature: 1852-2002," *Coord. Chem. Rev.*, vol. 251, no. 13-14 SPEC. ISS., pp. 1723–1733, 2007, doi: 10.1016/j.ccr.2006.12.015.
- [4] K. Liu *et al.*, "The development of micro-gyroscope technology," *J. Micromechanics Microengineering*, vol. 19, no. 11, 2009, doi: 10.1088/0960-1317/19/11/113001.
- [5] B. Mashadi, M. Mokhtari-Alehashem, and H. Mostaghimi, "Active vehicle rollover control using a gyroscopic device," *Proc. Inst. Mech. Eng. Part D J. Automob. Eng.*, vol. 230, no. 14, pp. 1958–1971, 2016, doi: 10.1177/0954407016641322.
- [6] G. K. Balachandran, V. P. Petkov, T. Mayer, and T. Balslink, "A 3-axis gyroscope for electronic stability control with continuous self-test," *IEEE J. Solid-State Circuits*, vol. 51, no. 1, pp. 177–186, 2016, doi: 10.1109/JSSC.2015.2496360.
- [7] Y. Li, F. Gu, G. Harris, A. Ball, N. Bennett, and K. Travis, "The measurement of instantaneous angular speed," *Mech. Syst. Signal Process.*, vol. 19, no. 4, pp. 786–805, 2005, doi: 10.1016/j.ymssp.2004.04.003.
- [8] B. Barshan and H. F. Durrant-Whyte, "Evaluation of a Solid-State Gyroscope for Robotics Applications," *IEEE Trans. Instrum. Meas.*, vol. 44, no. 1, pp. 61–67, 1995, doi: 10.1109/19.368102.
- [9] J. I. Thomas and J. Oliensis, "Automatic position estimation of a mobile robot," *Proc. Conf. Artif. Intell. Appl.*, pp. 438–444, 1993, doi: 10.1109/caia.1993.366634.
- [10] G. A. Abhinav, A. Shirur, D. Kannur, H. Bagewadi, and C. Vaidyanathan, "Improvements in the sensitivity of mems based gyroscope for military applications," *2020 7th Int. Conf. Signal Process. Integr. Networks, SPIN 2020*, pp. 483–488, 2020, doi: 10.1109/SPIN48934.2020.9070932.
- [11] C. W. Tan, S. Park, K. Mostov, and P. Varaiya, "Design of gyroscope-free navigation systems," *IEEE Conf. Intell. Transp. Syst. Proceedings, ITSC*, pp. 286–291, 2001, doi: 10.1109/itsc.2001.948670.
- [12] S. Oho, H. Kajioka, and T. Sasayama, "Optical Fiber Gyroscope for Automotive Navigation," *IEEE Trans. Veh. Technol.*, vol. 44, no. 3, pp. 698–705, 1995, doi: 10.1109/25.406639.
- [13] C. Barthold, K. Pathapati Subbu, and R. Dantu, "Evaluation of gyroscope-embedded mobile phones," *Conf. Proc. - IEEE Int. Conf. Syst. Man Cybern.*, pp. 1632–1638, 2011, doi: 10.1109/ICSMC.2011.6083905.

- [14] B. Delporte, L. Perroton, T. Grandpierre, and J. Trichet, “Accelerometer and magnetometer based gyroscope emulation on smart sensor for a virtual reality application,” *Sensors and Transducers*, vol. 14, no. SPEC. 1, pp. 32–47, 2012.
- [15] D. Zec, “The Sokol Movement from Yugoslav Origins to King Aleksandar’s 1930 All-Sokol Rally in Belgrade,” *East Cent. Eur.*, vol. 42, no. 1, pp. 48–69, 2015, doi: 10.1163/18763308-04201003.
- [16] V. Huttunen and R. Piché, “A Monocular camera gyroscope1,” *Gyroscopy Navig.*, vol. 3, no. 2, pp. 124–131, 2012, doi: 10.1134/S2075108712020046.
- [17] J. Belfi *et al.*, “A 1.82 m 2 ring laser gyroscope for nano-rotational motion sensing,” *Appl. Phys. B Lasers Opt.*, vol. 106, no. 2, pp. 271–281, 2012, doi: 10.1007/s00340-011-4721-y.
- [18] C. Verplaetse, “Inertial proprioceptive sensing toys and tools,” vol. 35, 1996.
- [19] H. Su, Y. Li, and L. Liu, *Gesture Recognition Based on Accelerometer and Gyroscope and Its Application in Medical and Smart Homes*, vol. 11268 LNCS. Springer International Publishing, 2018.
- [20] https://www.epsondevice.com/en/information/technical_info/gyro/
- [21] W. Tobin and B. Pippard, “Foucault, his pendulum and the rotation of the earth,” *Interdiscip. Sci. Rev.*, vol. 19, no. 4, pp. 326–337, 1994, doi: 10.1179/isr.1994.19.4.326.
- [22] A. Lawrence, “The Principles of Mechanical Gyroscopes,” *Mod. Inert. Technol.*, pp. 84–92, 1993, doi: 10.1007/978-1-4684-0444-9_7.
- [23] R. Usubamatov, “Mathematical model for gyroscope effects,” *AIP Conf. Proc.*, vol. 1660, 2015, doi: 10.1063/1.4915651.
- [24] A. Sharon and S. Lin, “Development of an automated fiber optic winding machine for gyroscope production,” *Robot. Comput. Integr. Manuf.*, vol. 17, no. 3, pp. 223–231, 2001, doi: 10.1016/S0736-5845(00)00030-2.
- [25] B. Culshaw, “The optical fibre Sagnac interferometer: An overview of its principles and applications,” *Meas. Sci. Technol.*, vol. 17, no. 1, 2006, doi: 10.1088/0957-0233/17/1/R01.
- [26] B. Wu, Y. Yu, J. Xiong, and X. Zhang, “Silicon Integrated Interferometric Optical Gyroscope,” *Sci. Rep.*, vol. 8, no. 1, pp. 1–7, 2018, doi: 10.1038/s41598-018-27077-x.
- [27] E. J. Post, “Sagnac effect,” *Rev. Mod. Phys.*, vol. 39, no. 2, pp. 475–493, 1967, doi: 10.1103/RevModPhys.39.475.
- [28] S. Sunada, S. Tamura, K. Inagaki, and T. Harayama, “Ring-laser gyroscope without the lock-in phenomenon,” *Phys. Rev. A - At. Mol. Opt. Phys.*, vol. 78, no. 5, pp. 1–8, 2008, doi: 10.1103/PhysRevA.78.053822.
- [29] C. H. Rowe, U. K. Schreiber, S. J. Cooper, B. T. King, M. Poulton, and G. E. Stedman, “Design and operation of a very large ring laser gyroscope,” *Appl. Opt.*, vol. 38, no. 12, p. 2516, 1999, doi: 10.1364/ao.38.002516.
- [30] H. C. Lefèvre, “Fundamentals of the interferometric fiber-optic gyroscope,” *Opt. Rev.*, vol. 4, no. 1 PART A, pp. 20–27, 1997, doi: 10.1007/bf02935984.
- [31] K. Ma, N. Song, J. Jin, J. He, and E. Zio, “Configuration Optimization in

- Miniature Interferometric Fiber-Optic Gyroscopes for Space Application,” *IEEE Sens. J.*, vol. 20, no. 13, pp. 7107–7117, 2020, doi: 10.1109/JSEN.2020.2977584.
- [32] J. Nayak, “Fiber-optic gyroscopes: From design to production [Invited],” *Appl. Opt.*, vol. 50, no. 25, 2011, doi: 10.1364/AO.50.00E152.
- [33] A. PR, P. S S, and R. Nambiar, “A Survey on Ring Laser Gyroscope Technology,” *Int. J. Comput. Appl.*, vol. 116, no. 2, pp. 25–27, 2015, doi: 10.5120/20310-2354.
- [34] W. M. MacEk and D. T. M. Davis, “Rotation rate sensing with traveling-wave ring lasers,” *Appl. Phys. Lett.*, vol. 2, no. 3, pp. 67–68, 1963, doi: 10.1063/1.1753778.
- [35] K. Suzuki, Y. Uehara, and H. Watanabe, “Ring Laser Gyro,” *J. Japan Soc. Precis. Eng.*, vol. 54, no. 2, pp. 289–292, 1988, doi: 10.2493/jjspe.54.289.
- [36] N. Beverini *et al.*, “Toward the ‘perfect square’ ring laser gyroscope,” *2014 Fotonica AEIT Ital. Conf. Photonics Technol. Fotonica AEIT 2014*, 2014, doi: 10.1109/Fotonica.2014.6843890.
- [37] A. H. Systems, P. Technology, and M. Station, “P . o .,” pp. 31–35, 1990.
- [38] M. Oh, M. Chung, and Y. Kim, “Open-loop fiber-optic gyroscope using intensity-modulated source and phase modulation,” *Opt. Lett.*, vol. 13, no. 6, p. 521, 1988, doi: 10.1364/ol.13.000521.
- [39] Z. Li, S. Gao, L. Jin, H. Liu, Y. Guan, and S. Peng, “Design and mechanical sensitivity analysis of a MEMS tuning fork gyroscope with an anchored leverage mechanism,” *Sensors (Switzerland)*, vol. 19, no. 16, 2019, doi: 10.3390/s19163455.
- [40] N. Abbate, A. Basile, C. Brigante, and A. Faulisi, “Development of a MEMS based wearable motion capture system,” *Proc. - 2009 2nd Conf. Hum. Syst. Interact. HSI '09*, pp. 255–259, 2009, doi: 10.1109/HSI.2009.5090988.
- [41] A. K. Brown and Y. Lu, “Performance test results of an integrated GPS/MEMS inertial navigation package,” *Proc. 17th Int. Tech. Meet. Satell. Div. Inst. Navig. ION GNSS 2004*, no. September, pp. 825–832, 2004.
- [42] A. A. Trusov, “Overview of MEMS Gyroscopes : History , Principles of Operations , Types of Measurements,” *Univ. California, Irvine, USA, maj*, no. May, pp. 1–15, 2011.
- [43] A. Das, N. Borisov, and M. Caesar, “Exploring Ways To Mitigate Sensor-Based Smartphone Fingerprinting,” 2015, [Online]. Available: <http://arxiv.org/abs/1503.01874>.
- [44] D. Piyabongkarn, R. Rajamani, and M. Greminger, “The development of a MEMS gyroscope for absolute angle measurement,” *IEEE Trans. Control Syst. Technol.*, vol. 13, no. 2, pp. 185–195, 2005, doi: 10.1109/TCST.2004.839568.
- [45] C. Patel and P. McCluskey, “Modeling and simulation of the MEMS vibratory gyroscope,” *Intersoc. Conf. Therm. Thermomechanical Phenom. Electron. Syst. IThERM*, pp. 928–933, 2012, doi: 10.1109/ITHERM.2012.6231524.

- [46] E. N. Pyatishhev, Y. B. Enns, A. N. Kazakin, R. V. Kleimanov, A. V. Korshunov, and N. Y. Nikitin, "MEMS GYRO comb-shaped drive with enlarged capacity gradient," *2017 24th Saint Petersburg. Int. Conf. Integr. Navig. Syst. ICINS 2017 - Proc.*, pp. 3–5, 2017, doi: 10.23919/ICINS.2017.7995647.
- [47] V. T. Dau, D. V. Dao, T. Shiozawa, H. Kumagai, and S. Sugiyama, "Development of a dual-axis thermal convective gas gyroscope," *J. Micromechanics Microengineering*, vol. 16, no. 7, pp. 1301–1306, 2006, doi: 10.1088/0960-1317/16/7/026.
- [48] P. T. Hoa, T. X. Dinh, and V. T. Dau, "Design Study of Multidirectional Jet Flow for a Triple-Axis Fluidic Gyroscope," *IEEE Sens. J.*, vol. 15, no. 7, pp. 4103–4113, Jul. 2015, doi: 10.1109/JSEN.2015.2411631.
- [49] V. T. Dau, T. Otake, T. X. Dinh, and S. Sugiyama, "Design and fabrication of convective inertial sensor consisting of 3DOF gyroscope and 2DOF accelerometer," *TRANSDUCERS 2009 - 15th Int. Conf. Solid-State Sensors, Actuators Microsystems*, pp. 1170–1173, 2009, doi: 10.1109/SENSOR.2009.5285911.
- [50] J. Bahari, R. Feng, and A. M. Leung, "Robust MEMS Gyroscope Based on Thermal Principles," *J. Microelectromechanical Syst.*, vol. 23, no. 1, pp. 100–116, Feb. 2014, doi: 10.1109/JMEMS.2013.2262584.
- [51] G. Kock, P. Combette, M. Tedjini, M. Schneider, C. Gauthier-Blum, and A. Giani, "Experimental and numerical study of a thermal expansion gyroscope for different gases," *Sensors (Switzerland)*, vol. 19, no. 2, 2019, doi: 10.3390/s19020360.
- [52] S. Q. Liu and R. Zhu, "Micromachined fluid inertial sensors," *Sensors (Switzerland)*, vol. 17, no. 2, 2017, doi: 10.3390/s17020367.
- [53] T. Shiozawa, T. Van Dau, D. V. Dao, H. Kumagai, and S. Sugiyama, "A dual axis thermal convective silicon gyroscope," *Proc. 2004 Int. Symp. Micro-NanoMechatronics Hum. Sci. MHS2004; Fourth Symp. 'Micro-NanoMechatronics Information-Based Soc. 21st Century*, pp. 277–282, 2004, doi: 10.1109/mhs.2004.1421318.
- [54] R. Zhu, S. Cai, H. Ding, Y. J. Yang, and Y. Su, "A micromachined gas inertial sensor based on thermal expansion," *Sensors Actuators, A Phys.*, vol. 212, pp. 173–180, 2014, doi: 10.1016/j.sna.2014.01.041.
- [55] C. Marshall, E. Matlis, T. Corke, and S. Gogineni, "AC plasma anemometer - Characteristics and design," *Meas. Sci. Technol.*, vol. 26, no. 8, pp. 0–28, 2015, doi: 10.1088/0957-0233/26/8/085902.
- [56] A. P. Chattock, "Magazine journal of science.," *London, Edinburgh, Dublin Philos. Mag. J. Sci.*, vol. 48, no. 294, pp. 401–420, 1899.
- [57] M. Robinson, "Movement of A i r in the Electric W i n d oí the Corona Discharge."
- [58] M. Rickard, D. Dunn-Rankin, F. Weinberg, and F. Carleton, "Characterization of ionic wind velocity," *J. Electrostat.*, vol. 63, no. 6–10, pp. 711–716, 2005, doi: 10.1016/j.elstat.2005.03.033.
- [59] J. Wilson, H. Perkins, and W. Thompson, "An Investigation of Ionic Wind

- Propulsion,” *NASA Rep. NASA/TM*, no. 215822, pp. 1–36, 2009.
- [60] D. Cagnoni, F. Agostini, T. Christen, N. Parolini, I. Stevanović, and C. De Falco, “Multiphysics simulation of corona discharge induced ionic wind,” *J. Appl. Phys.*, vol. 114, no. 23, 2013, doi: 10.1063/1.4843823.
 - [61] V. T. Dau, T. X. Dinh, T. Terebessy, and T. T. Bui, “Bipolar corona discharge based air flow generation with low net charge,” *Sensors Actuators, A Phys.*, vol. 244, pp. 146–155, 2016, doi: 10.1016/j.sna.2016.03.028.
 - [62] E. Moreau, L. Léger, and G. Touchard, “Effect of a DC surface-corona discharge on a flat plate boundary layer for air flow velocity up to 25 m/s,” *J. Electrostat.*, vol. 64, no. 3–4, pp. 215–225, 2006, doi: 10.1016/j.elstat.2005.05.009.
 - [63] E. Moreau, C. Louste, and G. Touchard, “Electric wind induced by sliding discharge in air at atmospheric pressure,” *J. Electrostat.*, vol. 66, no. 1–2, pp. 107–114, 2008, doi: 10.1016/j.elstat.2007.08.011.
 - [64] D. G. Mohan *et al.*, “Accepted Manuscript,” *Mater. Today Proc.*, vol. 27, no. xxxx, pp. 0–31, 2019, doi: 10.1080/14484846.2018.1432089.
 - [65] Y. Zhang, L. Liu, Y. Chen, and J. Ouyang, “Characteristics of ionic wind in needle-to-ring corona discharge,” *J. Electrostat.*, vol. 74, no. December 2014, pp. 15–20, 2015, doi: 10.1016/j.elstat.2014.12.008.
 - [66] R. Ono and T. Oda, “Dynamics of ozone and OH radicals generated by pulsed corona discharge in humid-air flow reactor measured by laser spectroscopy,” *J. Appl. Phys.*, vol. 93, no. 10 1, pp. 5876–5882, 2003, doi: 10.1063/1.1567796.
 - [67] S. Masuda and H. Nakao, “Control of NO_x by Positive and Negative Pulsed Corona Discharges,” *IEEE Trans. Ind. Appl.*, vol. 26, no. 2, pp. 374–383, 1990, doi: 10.1109/28.54266.
 - [68] L. A. Rosenthal and D. A. Davis, “Electrical Characterization of a Corona Discharge for Surface Treatment,” *IEEE Trans. Ind. Appl.*, vol. IA-11, no. 3, pp. 328–335, 1975, doi: 10.1109/TIA.1975.349324.
 - [69] E. Moreau, N. Benard, J. D. Lan-Sun-Luk, and J. P. Chabriat, “Electrohydrodynamic force produced by a wire-to-cylinder dc corona discharge in air at atmospheric pressure,” *J. Phys. D. Appl. Phys.*, vol. 46, no. 47, 2013, doi: 10.1088/0022-3727/46/47/475204.
 - [70] V. T. Dau, T. T. Bui, T. X. Dinh, and T. Terebessy, “Pressure sensor based on bipolar discharge corona configuration,” *Sensors Actuators, A Phys.*, vol. 237, pp. 81–90, 2016, doi: 10.1016/j.sna.2015.11.024.
 - [71] N. T. Van *et al.*, “A Circulatory Ionic Wind for Inertial Sensing Application,” *IEEE Electron Device Lett.*, vol. 40, no. 7, pp. 1182–1185, Jul. 2019, doi: 10.1109/LED.2019.2916478.
 - [72] Z. Yi, M. Qin, and Q.-A. Huang, *A Micromachined Thermal Wind Sensor*. 2018.
 - [73] A. Morgenshtein, L. Sudakov-Boreysha, U. Dinnar, C. G. Jakobson, and Y. Nemirovsky, “Wheatstone-Bridge readout interface for ISFET/REFET applications,” *Sensors Actuators, B Chem.*, vol. 98, no. 1, pp. 18–27, 2004,

- doi: 10.1016/j.snb.2003.07.017.
- [74] R. W. Clough, “Original formulation of the finite element method,” *Finite Elem. Anal. Des.*, vol. 7, no. 2, pp. 89–101, 1990, doi: 10.1016/0168-874X(90)90001-U.
 - [75] E. Yamaguchi, “Finite element method,” *Bridg. Eng. Handb. Fundam. Second Ed.*, pp. 225–251, 2014, doi: 10.1201/b15616.
 - [76] F. Elements, I. N. Analysis, and A. N. D. Design, “Pre- and post-processing for the finite element method,” vol. 19, pp. 243–260, 1995.
 - [77] Hang Nguyen Thu, Ngoc Tran Van, Van Dau Thanh, Tung Bui Thanh, Cuong Nguyen Nhu, Trinh Chu Duc and An Nguyen Ngoc, “Study on Thermal Convective Gas Gyroscope based on Corona Discharge Ion Wind and Coriolis Effect”, International Conference on Engineering Research and Applications, Dec. 2020, Lecture Notes in Networks and Systems, vol 178. Springer, Cham.
 - [78] <https://www.comsol.com/>
 - [79] <https://looseendsbrewing.com/beers/coriolis-effect/>
 - [80] Kufre Esenowo Jack and Emmanuel O. Nwangwu and I. Etu and E. U. Osuagwu, A Simple Thermistor Design for Industrial Temperature Measurement, IOSR Journal of Electrical and Electronics Engineering, vol 11, pp. 57-66, 2016.
 - [81] <https://slideplayer.com/slide/10817714/>